

# **The Productora Cu-Au-Mo deposit, Chile: A Mesozoic magmatic-hydrothermal breccia complex with both porphyry and IOCG affinities**

Angela Escolme<sup>1\*</sup>, David R. Cooke<sup>1</sup>, Julie Hunt<sup>2</sup>, Ron F. Berry<sup>1</sup>, Roland Maas<sup>3</sup>, Robert A. Creaser<sup>4</sup>

<sup>1</sup>ARC Research Hub for Transforming the Mining Value Chain & CODES, University of Tasmania, Hobart, TAS, Australia, 7001

<sup>2</sup>CODES, University of Tasmania, Hobart, TAS, Australia, 7001

<sup>3</sup>School of Earth Sciences, University of Melbourne, Melbourne, Victoria 3010, Australia

<sup>4</sup>Department of Earth and Atmospheric Sciences, University of Alberta, Edmonton, AB, T6G 2R3, Canada

\*corresponding author

Address: ARC Research Hub for Transforming the Mining Value Chain (TMVC), Centre for Ore Deposit and Earth Sciences (CODES), University of Tasmania, Private Bag 79, Hobart, TAS, 7001, Australia

Email: [angela.escolme@utas.edu.au](mailto:angela.escolme@utas.edu.au)

Telephone: +61 3 6226 2664

## Abstract

The Productora Cu-Au-Mo deposit is hosted by a Cretaceous hydrothermal breccia complex in the Coastal Cordillera of northern Chile. The current resource, which includes the neighboring Alice Cu-Mo porphyry deposit, is estimated at 236.6 Mt grading 0.48 % Cu, 0.10 g/t Au and 135 ppm Mo. Local wall rocks consist of a thick sequence of broadly coeval rhyolite to rhyodacite lapilli tuffs ( $128.7 \pm 1.3$  Ma; U-Pb<sub>zircon</sub>) and two major intrusions; the Cachiuyuyito tonalite and Ruta Cinco granodiorite batholith ( $92.0 \pm 1.0$  Ma; U-Pb<sub>zircon</sub>). Previous studies at Productora concluded the deposit had strong affinities with the IOCG clan and likened the deposit to Candelaria. Based on new information, we document the deposit geology in detail and propose a new genetic model and alternative classification as a magmatic-hydrothermal breccia complex with closer affinities to porphyry systems.

Hydrothermal and tectonic breccias, veins and alteration assemblages at Productora define five paragenetic stages: stage 1 quartz - pyrite-cemented breccias associated with muscovite alteration, stage 2 chaotic matrix-supported tectonic-hydrothermal breccia with kaolinite – muscovite – pyrite alteration, stage 3 tourmaline – pyrite – chalcopyrite  $\pm$  magnetite  $\pm$  biotite-cemented breccias and associated K-feldspar  $\pm$  albite alteration, stage 4 chalcopyrite  $\pm$  pyrite  $\pm$  muscovite, illite, epidote and chlorite veins, and stage 5 calcite veins. The Productora hydrothermal system crosscuts earlier-formed sodic-calcic alteration and magnetite-apatite mineralization associated with the Cachiuyuyito stock. Main stage mineralization at Productora was associated with formation of the stage 3 hydrothermal breccia. Chalcopyrite is the dominant hypogene Cu mineral and occurs predominantly as breccia cement and syn-breccia veins with pyrite.

The Alice Cu-Mo deposit is characterized by disseminated chalcopyrite and quartz – pyrite – chalcopyrite  $\pm$  molybdenite vein stockworks hosted by a granodiorite porphyry stock. Alice is spatially associated with the Silica Ridge lithocap, which is characterized by massive, fine grained quartz-altered rock above domains of alunite, pyrophyllite and dickite. Rhenium-Os dating of molybdenite indicates that main stage mineralization at Productora occurred at  $130.1 \pm 0.6$  Ma, and at  $124.1 \pm 0.6$  Ma in the Alice porphyry.

Chalcopyrite and pyrite from Productora have  $\delta^{34}\text{S}_{\text{sulfide}}$  values from -8.5 to +2.2 ‰, consistent with a magmatic sulfur source and fluids evolving under oxidizing conditions. No significant input from evaporite- or seawater-sourced fluids was detected. Stage 3 tourmalines have average initial Sr of 0.70397, consistent with an igneous-derived Sr source.

The Productora magmatic-hydrothermal breccia complex formed as a result of explosive volatile fluid release from a hydrous intrusive complex. Metal-bearing fluids were of magmatic affinity and evolved under oxidizing conditions. Despite sharing many similarities with the Andean IOCG clan (strong structural control, regional sodic-calcic alteration, locally anomalous U), fluid evolution at the Productora Cu-Au-Mo deposit is more consistent with that of a porphyry-related magmatic hydrothermal breccia (sulfur-rich, acid alteration assemblages and relatively low magnetite contents, <5 vol%). The Productora camp is an excellent example of the close spatial association of Mesozoic magnetite-apatite, porphyry and magmatic-hydrothermal breccia mineralization styles, a relationship seen throughout the Coastal Cordillera of northern Chile.

## Introduction

Iron-oxide copper gold (IOCG) deposits have been the subject of much research and controversy, particularly in regard to their origin and association to other deposit styles. Debate has largely centered around fluid source, and both magmatic-hydrothermal (e.g., Hitzman et al., 1992; Pollard, 2000; Sillitoe, 2003; Richards and Mumin, 2013a, b) and external ‘basinal’ brine models have been proposed (Barton and Johnson, 1996; Hitzman, 2000). Magnetite-apatite, or iron-oxide apatite (IOA) deposits have been described as a copper-poor end-members of the IOCG clan (e.g., Barton, 2014), with some authors proposing they represent the deeper root zones of IOCG systems (Espinoza et al. 1996, Sillitoe, 2003). Discussion on the genesis of magnetite-apatite deposits is similarly controversial owing largely to the variety of observed characteristics. Proposed genetic models vary in iron oxide source, from immiscible iron-rich melts (Nyström and Henríquez, 1994; Naslund et al., 2002; Henríquez et al., 2003), to purely hydrothermal magnetite with magmatic (e.g., Pollard, 2000 and 2001, Barra et al. 2016) and/or basinal fluid sources (e.g., Menard, 1995; Barton and Johnson, 1996; Rhodes and Oreskes, 1999; Rhodes et al., 1999; Sillitoe and Burrows, 2002). In more recent times, a novel hypothesis invoking both buoyant igneous magnetite concentration by flotation with hydrothermal magnetite deposition has been proposed (Knipping et al. 2015a, b, Reich et al. 2016, Simon et al. 2018).

In the Mesozoic Coastal Cordillera of northern Chile, IOCG, magnetite-apatite and porphyry-Cu deposits all share a close temporal and spatial association. The relationship between these deposit styles in the region has been explored by several workers seeking to understand controls on their formation (Sillitoe, 2003; Williams et al., 2005; Chen, 2010; Tornos et al., 2010; Richards et al., 2017), and possible relationships between deposits styles. The spatial association of adjacent magnetite- and hematite-dominated IOA deposits has been cited as evidence for zonal relationship between deep proximal magnetite and shallow distal hematite (e.g., Manto Verde and Manto Ruso; Rieger et al., 2012). Although no transitions have been documented between Chilean magnetite-apatite and IOCG deposits, Sillitoe (2003) proposed that magnetite-apatite deposits may occur at depth below magnetite-dominated IOCGs, and that a transition may occur where Cu content of the



IOCG ores decreases with depth. However, IOCG deposits in the Coastal Cordillera are mostly 170 and 110 Ma (Sillitoe, 2003; Chen, 2010) whereas IOA deposits are typically 128 to 102 Ma (Oyarzun et al., 2003). Porphyry deposits in the Coastal Cordillera largely overlap in age with the IOA deposits, and range between 132 and 97 Ma (Maksaev et al. 2007). The Punta del Cobre district has been proposed as intermediate between magnetite-apatite and porphyry-Cu deposit (Marschik and Fontboté, 1996), whereas the Tropezón Cu-Mo-(Au) deposit in northern Chile is described as an IOCG deposit with porphyry features that demonstrates a genetic relationship between the deposit classes (Tornos et al., 2010). This close spatial association between magnetite-apatite and porphyry-style mineralization is also observed at a camp scale at Productora.

The Productora Cu-Au-Mo deposit is hosted by a tourmaline-cemented breccia complex in the Chilean Coastal Cordillera (Fig. 1). Productora has been described by previous authors to have mineralization and alteration features compatible with the IOCG model and has been likened to Candelaria on the basis of pervasive potassic alteration, presence of significant magnetite and chalcopyrite, structural setting and age (Fox, 2000; Ray and Dick 2002). This work was largely based on surface mapping and a limited number of shallow drill holes. It is also noteworthy that the project was previously explored for U during the 1980's by the Chilean Commission for Nuclear Energy, who defined a shallow  $U_3O_8$  resource (Table 1). Our work, benefitting from significantly more drill hole data, has shown that although the deposit has features compatible with both the IOCG and porphyry model, the latter is favored. This is largely based on evidence for magmatic-hydrothermal fluid evolution (sulfur-rich with acid alteration assemblages) and relatively low iron-oxide contents (<5 vol% magnetite). We also find that the Productora deposit is significantly older than previously reported. The presence and timing relationships of neighboring magnetite-apatite and porphyry-Cu-Au-Mo prospects make Productora a deposit of significance in the ongoing debate over possible relationships between these mineralization types.

This paper documents the geology, alteration, and mineralization of the Productora Cu-Au-Mo deposit and provides insights into its hydrothermal evolution through stable and radiogenic isotopic studies. Results from the current study, and those of previous workers, are synthesized into a

new genetic model for Productora. The relevance of both porphyry and IOCG models for Productora are assessed, as are potential mineralizing fluid sources.

## **Methods**

Geological descriptions in this study are largely based on observations from surface mapping, diamond drill core logging (16 drill holes were examined for 2,797 m), transmitted and reflected light petrography, SWIR analysis (data collected using ASD Terraspec instrument at CODES, University of Tasmania and interpreted using The Spectral Geologist Professional© version 5.03.002), feldspar staining, and review of previous work. Note local and regional maps are based on the work of previous authors who are referenced accordingly. Cross sections have been constructed at 6,822,215 mN and 6,820,850 mN based on graphic logging (following the methods of McPhie et al., 1993 and Blackwell, 2010), core photography (19 drill holes for 6,083 m) and whole rock immobile element lithogeochemistry. Sample locations provided in Appendix 1.

### ***U-Pb geochronology***

Six samples were submitted to CODES, University of Tasmania for geochronological analysis by U-Pb method through the laser ablation inductively coupled mass spectrometry (LA-ICP-MS) method on zircons. Samples were crushed to <400 µm and zircons hand picked from a non magnetic heavy mineral separate. Zircon grains were mounted in epoxy resin, and reviewed under cathode luminescence at the Central Sciences Laboratory, University of Tasmania in order to check for inheritance. Analysis of U-Pb was performed on suitable grains using an Agilent 7900 quadrupole ICP-MS with 193 mm coherent Ar-F excimer laser and Resonetics S155 ablation cell. Further method details are provided in Appendix 2. In most cases little to no inheritance was observed in the data and results plotted on concordia. Analyses which showed evidence of Pb loss or common lead were excluded from the age calculations. Results are presented in the following text, supporting data provided in Appendix 3.

### ***Re-Os geochronology***

Two drill core samples were prepared for mineral separation and dated using Re-Os geochronology techniques at University of Alberta Radiogenic Isotope Facility, Canada. For each sample, a molybdenite mineral separate was created through metal-free crushing followed by gravity and magnetic concentration methods described in detail by Selby and Creaser (2004). The concentrations of  $^{187}\text{Re}$  and  $^{187}\text{Os}$  in molybdenite were determined by isotope dilution mass spectrometry using Carius-tube, solvent extraction, anion chromatography and negative thermal ionization mass spectrometry techniques. A mixed double spike containing known amounts of isotopically enriched  $^{185}\text{Re}$ ,  $^{190}\text{Os}$ , and  $^{188}\text{Os}$  analysis was used (Markey et al. 2007). Isotopic analysis was made using a ThermoScientific Triton mass spectrometer by Faraday collector. Total blanks for Re and Os are less than <3 picograms and 2 picograms, respectively, which are insignificant for the Re and Os concentrations in molybdenite. The molybdenite powder HLP-5 (Markey et al., 1998), was analyzed as a standard. Over a period of two years, the HLP-5 standard has yielded an average Re-Os date of  $221.56 \pm 0.40$  Ma (1SD uncertainty,  $n=10$ ). This Re-Os age date is identical to that reported by Markey et al. (1998) of  $221.0 \pm 1.0$  Ma.

### ***S isotopes***

Sulfur isotope compositions in the current study were determined for 48 paragenetically constrained mineral samples from Productora. The sample suite included 25 pyrite samples, 21 chalcopyrite, one molybdenite sample and one anhydrite sample. Samples were predominantly sourced from cross sections 6,822,215 mN ( $n=27$ ) and 6,820,850 mN ( $n=19$ ), with two from a central section at 6,821,730 mN. Monomineralic powders (~10 mg) were prepared by hand drilling directly from in-situ coarse grain sulfide minerals using a Dremel Multipro 225 T2 Flex-shaft drill. The drill bit was cleaned between samples using a chalk block. Powders were transferred on clean weighing paper into a vial and weighed to check that the minimum sample requirement had been met. Samples were analysed at the Central Science Laboratory, University of Tasmania, Australia, for sulfur isotope composition. Analyses were performed on sub-samples, weighing <1 mg, by conventional isotope ratio mass spectrometry methods using an Isoprime100 mass spectrometer coupled to an Elementar vario PYRO cube elemental analyzer. Seven international standards (IAEA-

S-1, -2 and -3, IAEA-SO-6 and -7, and NBS127) were also collected and results are reported with reference to the Canyon Diablo Troilite (CDT  $\delta^{34}\text{S} = 0.0\%$ ) international standard.

### ***Sr isotopes***

Strontium isotope analysis was performed on nine tourmaline mineral separates. Samples were selected based predominantly on the presence of coarse tourmaline and secondly on the spatial distribution across the deposit, including examples of proximal, distal, shallow and deep locations. Samples were crushed with a mortar and pestle and sieved for the 250-500  $\mu\text{m}$  size fraction. A strong magnet was used to separate iron rich phases (tourmaline and pyrite) from quartz-feldspar rich grains. Grains were then washed in tap water and dried at 60 degrees for two hours. Tourmaline grains were separated using a binocular microscope.

Strontium isotope compositions of bulk tourmalines were determined at the University of Melbourne. Eight small ( $\leq 3$  mg) tourmaline concentrates were ground to powder in an agate mortar, rinsed in distilled water and transferred to Krogh-type high-pressure PTFE vessels. Due to the small sample sizes and the possible presence of residual moisture, no sample weights were determined. After a brief acid leach with warm 0.5M  $\text{HNO}_3$  to remove easily soluble impurities (carbonates, apatite), the tourmaline residues were dissolved at high pressure (3:1  $\text{HF-HNO}_3$ , 160°C, 48 hrs). Fluorides were destroyed with concentrated  $\text{HNO}_3$ , followed by a second high-pressure stage with 6M  $\text{HNO}_3$ . Small splits of the clear solutions were removed for trace element analysis on an Agilent 7700x quadrupole ICP-MS; the remainder was used for Sr extraction using a single pass over small (0.15 ml) columns of Eichrom Sr resin. Sr isotope data were acquired on a Nu Plasma MC-ICP-MS (e.g. Maas et al., 2015). Instrumental mass bias was corrected by internal normalization to  $^{88}\text{Sr}/^{86}\text{Sr} = 8.37521$  using the exponential law, and  $^{87}\text{Sr}/^{86}\text{Sr}$  is reported relative to  $\text{SRM987} = 0.710230$ .  $^{87}\text{Rb}/^{87}\text{Sr}$  ratios for age corrections were formed from the trace element data which are available as total nanograms rather than concentrations; the Rb decay constant is  $1.395 \times 10^{-11}/\text{yr}$ .

### **Regional setting**

The Mesozoic metallogenic belt, situated in the Coastal Cordillera of the central Andes, extends from southern Peru through northern to central Chile (13°–34°S; Sillitoe and Perelló, 2005). Arc magmatism along the South American continental margin was triggered by the initiation of eastward-directed subduction of the present day Nazca plate under South America during the late Paleozoic, marking the beginning of the Andean orogenic cycle (Coira et al. 1982; Mpodozis and Ramos, 1990). Extensional tectonics during the Mesozoic led to intense arc magmatism, accumulation of thick basin sediment sequences, and emplacement of large batholiths (Mpodozis and Ramos, 1990; Mpodozis and Allmendinger, 1993; Scheuber and Gonzalez, 1999; Charrier et al., 2007). The Chilean Coastal Batholith, a 1,200 km belt of orogen-parallel plutons that are typically <50 km in length, was emplaced contemporaneously with regional volcanism during the Jurassic and Early Cretaceous (Dallmeyer et al., 1996; Sillitoe, 2003; Vásquez et al. 2011). Extensional geodynamic conditions at that time have been attributed to a high-angle, oblique subduction regime that prevailed throughout the Jurassic and Early Cretaceous (Dallmeyer et al., 1996; Taylor et al., 1998; Scheuber and Gonzalez, 1999; Grocott and Taylor, 2002; Parada et al., 2007). Arc volcanism was widespread at this time, producing volcanic sequences that are several thousand meters thick and comparable in volume to the smaller examples of large igneous provinces (e.g., La Negra Formation; Sillitoe, 2003; Oliveros et al., 2006). Marine intercalations within the volcanic sequences and limited detritus in the back arc basin sediments provide evidence for local lowland topography (Vergara et al., 1995; Scheuber and Gonzalez, 1999). Eastward, the volcanic sequences are intercalated with carbonate and clastic sedimentary rocks of the Aconcagua platform, a narrow shelf formed along the stable continental margin (Mpodozis and Ramos, 1990). A range of deposit types are hosted in the Mesozoic volcano-sedimentary sequences, including small porphyry Cu, manto-type Cu, IOCG, and magnetite-apatite deposits (Sillitoe and Perelló, 2005; Fig. 1).

Volcanic and intrusive rocks of the Jurassic and Early Cretaceous magmatic arc are cross cut by the Atacama Fault System (AFS) — a north striking arc parallel fault system extending over 1,000 km from Iquique (20°S) to La Serena (~30°S; Brown et al., 1993; Sillitoe and Perello, 2005; Fig. 1). Development of the AFS was contemporaneous with formation of the Mesozoic arc in the Coastal

Cordillera (Brown et al., 1993) and is believed to have provided the structural architecture for magma ascent (Berg et al., 1983; Scheuber and Reutter, 1992; Grocott et al., 1994). The time-space association of arc magmatism with faulting is consistent with a transtensional tectonic environment with arc normal extension and strike-slip displacement (Hervé, 1987; Scheuber and Reutter, 1992; Brown et al., 1993).

Shallowing of the subduction angle during the Late Cretaceous led to severe deformation and crustal thickening, closure of back arc basins, eastward migration of the magmatic arc and transition to a compressional regime by the mid Tertiary (Barazangi and Isacks, 1979; Pilger, 1981; Mpodozis and Ramos, 1990; Ramos, 1999; Ramos and Folguera, 2009). The onset of this compressional tectonic regime caused volcanism to cease (Ramos, 1999) and led to more evolved magmas and diminished formation of IOCG, magnetite-apatite and manto-type Cu deposits (Sillitoe, 2003). The suppression in volcanism permitted large fluid-rich mantle derived magma chambers to form at relatively shallow crustal levels, producing large porphyry copper deposits during the Tertiary (Sillitoe and Perelló, 2005).

## **Results**

### ***Location and history***

Productora is situated in a drainage basin 600 to 900 m above sea level. The deposit is partially covered by Quaternary gravels. The nearest township is Vallenar, 17 km to the north. The Productora camp has a history of Cu, and Au mining, extending back to pre-Hispanic times. Historical Fe mining also occurred at La Chulula, La Bandera, Mariposa, Carmen, and La Negra mines (Fig. 2). Copper mining occurred in the region during the past century, and locally at Productora and Santa Inés (operated by Playa Brava), Remolina, and Montserrat mines. There are more than 80 small pits, workings, or mineralized outcrops in the project area containing Fe, Cu, or Au mineralization (Fox, 2000). Exploration activities at Productora, including exploration during the 1980's for U, are summarized in Table 1. Following acquisition of the tenement package in 2010, Hot Chili Ltd commenced an extensive 80 x 40 m drill out. Approximately 160,000 m of drilling were completed

over four years. A JORC compliant maiden resource of 214.3 Mt grading 0.48 % Cu, 0.1 g/t Au, and 138 ppm Mo was announced in March 2014 (Hot Chili Ltd, 2014). A pre-feasibility study was completed in early 2016 with an upgraded resource of 236.6 Mt grading 0.48 % Cu, 0.10 g/t Au and 135 ppm Mo (including Productora for 218.7 Mt grading 0.48 % Cu, 0.1 g/t Au and 142 ppm, and Alice porphyry for 17.9 Mt grading 0.41 Cu, 0.04 g/t Au and 39 ppm Mo; Hot Chili Ltd, 2016). Recent discoveries at the deposit include a series of Au-bearing veins located south of the Productora Cu-Au-Mo deposit and extensions to the Alice porphyry mineralization (Hot Chili Ltd, 2017).

Major features of the local geology at Productora include the Jurassic volcanic stratigraphy, two major intrusive bodies, a hydrothermal breccia complex, and a complex fault network (Fig. 2). During the course of this study, drill core predominantly from two cross sections through the deposit at 6,822,215 mN and 6,820,850 mN (Figs. 3 and 4) were reviewed and sampled as well as reconnaissance surface mapping of outcrop and drill pads.

### ***Volcanic Rocks***

Productora is hosted by the Bandurrias Formation (Segerstrom 1960; Moscoco et al., 1982), part of the Jurassic-Early Cretaceous magmatic arc (Charrier et al., 2007), and stratigraphically equivalent to the Punta del Cobre Formation to the north. Locally, the Bandurrias Group consists of early andesite-dacite tuffs overlain conformably by rhyodacite lapilli tuff and rhyodacite monomict breccia, rhyolite welded lapilli tuff, and rhyolite lapilli tuff, and unconformably by basalt and basalt-andesite flows (Fox, 2000; this study; Fig. 5). Complete volcanic rock descriptions and geochronology are summarized in Tables 2 and 3 respectively. Volcanic textures observed at Productora are consistent with an explosive subaerial magmatic arc environment that generated thick pyroclastic deposits and lava flows and/or domes (McPhie et al., 1993). Uranium-Pb<sub>zircon</sub> geochronology reveals that the volcanic stratigraphy was assembled between  $128.7 \pm 0.9$  Ma (rhyodacite lapilli tuff) and  $128.0 \pm 0.9$  Ma (rhyolite welded lapilli tuff; Table 3).

### ***Intrusive Rocks***

Four intrusive phases have been recognized at Productora and these have been dated using the U-Pb<sub>zircon</sub> method (Fig. 2, 6; Tables 3 and 4). From oldest to youngest, they are: Cachiyuyito tonalite-diorite ( $129.8 \pm 0.1$  Ma; Fox, 2000), Alice granodiorite porphyry ( $121.1 \pm 2.1$  Ma), Zapallo porphyry ( $118.9 \pm 0.9$  Ma), and Ruta Cinco batholith (quartz-monzonite border:  $96.1 \pm 0.2$  Ma; Fox 2000; granodiorite core:  $92.0 \pm 1.0$  Ma, this study). Geochronologic data from the volcanic rocks and Cachiyuyito intrusion are inconsistent with field observations as the volcanic host rocks return ages 0.1–1.16 Ma younger than the intrusion, considering uncertainty. Additional sampling and dating of the Cachiyuyito intrusion and volcanic sequence may resolve this discrepancy – although similar ages are to be expected given the coeval nature of volcanic and intrusive magmatism in the Jurassic to Early Cretaceous arc (Dallmeyer et al., 1996). Alternatively, since the volcanic rocks dated were sampled from the eastern side of the project, it is possible that these may have been downthrown from a shallower and younger part of the volcanic sequence. Field relationships indicate that the Cachiyuyito tonalite pre-dates mineralization at Productora (Fox, 2000). The Zapallo porphyry and Ruta Cinco batholith post-date both the Productora breccia complex.

### ***Structure***

Productora is located approximately 10 km to the east of the AFS (Fig. 1). The sinistral strike-slip AFS consists of many discontinuous and crosscutting faults. Overlapping faults define asymmetric, fault-bounded slabs interpreted to be sidewall rip-out structures (Brown et al., 1993; Taylor et al., 1998), jogs, and duplexes (Cembrano et al., 2005). At Productora, local structures are inferred to be subsidiary to the AFS (Fox, 2000; Ray and Dick, 2002; J. Beeson, pers. commun., 2012). There are three major north-northeast striking faults and three major northwest striking faults at Productora (Fig. 2). There are also numerous examples of minor northwest-, west-, and northeast-oriented faults that locally host diorite and porphyritic dacite dikes (Fox, 2000; Ray and Dick, 2002; J. Beeson, pers. commun., 2012). Northeast-striking faults are more common to the north of the deposit. The north-striking faults generally dip 60–80° west and have normal oblique-slip with sinistral strike-slip, and east-side up dip-slip movement (Fox, 2000). The northwest-striking faults, which are numerous, have normal oblique-slip with dextral strike-slip and northeast side up dip-slip movement.



The northwest-striking faults crosscut the north-striking fault set (Fig. 2; Fox, 2000; Ray and Dick, 2002; J. Beeson, pers. commun., 2012).

### **Alteration and mineralization**

The Productora district is characterized by a complex sequence of overprinted alteration assemblages. Hydrothermal activity began during emplacement of the Cachiyuyito tonalite-diorite, which generated sodic-calcic assemblages and magnetite-apatite mineralization. This was followed by the Productora hydrothermal system and associated Cu-Au-Mo mineralization; Alice porphyry intrusion, with associated porphyry-stage alteration and Cu-Mo mineralization, and the Silica Ridge lithocap; and the Ruta Cinco hydrothermal system, which produced propylitic alteration and gold-bearing veins (Fox, 2000; Ray and Dick, 2002; Table 5, Fig. 7). The Productora hydrothermal system consists of a sequence of hydrothermal breccias, tectonic breccias, veins, and alteration assemblages that have been separated into five paragenetic stages: stage 1 quartz-pyrite-cemented breccia; stage 2 chaotic matrix-supported breccia; stage 3 tourmaline breccias; stage 4 phyllic and propylitic veins; and stage 5 propylitic veins (Table 6). Stage 3 breccias have been further subdivided into subfacies based on cement mineralogy. The relationship between paragenetic stages at Productora and the broader camp scale parageneses is outlined in Figure 8. Spatial distribution of the breccia facies in cross section is presented in Figures 9 and 10.

### ***Cachiyuyito magnetite – apatite mineralization***

Magnetite – apatite mineralization occurs at the historic mines Mariposa, La Bandera, La Chulula, La Negrita and El Molle to the East of Productora (Fig. 7) and has been documented by previous authors Fox (2000) and Ray and Dick (2002). Magnetite mineralization occurs as pods, lenses (1-7 m wide), veins (0.5-15 cm), veinlets (<1-5 mm) or disseminated grains (<4 mm). Magnetite is commonly associated with actinolite and apatite within andesites adjacent to the sodic-calcic-altered Cachiyuyito intrusion. The andesites are pervasively altered to albite – chlorite – actinolite – magnetite with veins of chlorite – actinolite – magnetite – epidote. Pods and dikes of massive magnetite (Fig. 11A) and magnetite intergrown with coarse apatite and actinolite (Fig. 11B

and C), are common within 100 m of the contact with the Cachiyuyito intrusion. Where apatite is abundant, veins of apatite and coarse actinolite mutually cross cut each other (Fox, 2000). Cross cutting relationships provide evidence that the Cachiyuyito magnetite-apatite mineralization pre-dates the Productora breccia complex and Cu mineralization (Fig. 11D; Fox, 2000).

### ***Productora breccia complex - veins and hydrothermal breccias***

#### ***Stage 1 quartz-pyrite-cemented breccia:***

The earliest recognized hydrothermal feature at Productora is stage 1 massive, matrix supported, chaotic, poorly sorted, quartz-pyrite cemented, polymict lithic breccia (Fig. 12A, Table 6). The breccia is broadly distributed across the deposit, estimated to be >400 m wide, 1,300 m long, and at least 300 m in thickness. Individual clasts have porphyritic (Fig. 12B) or clastic texture, which suggest a volcanic protolith and multiple brecciation events. The quartz cement is massive and microcrystalline with disseminated pyrite (1–2 vol%; 0.05–0.3 mm; Fig. 12B). No significant Cu, Au, or Mo mineralization is associated with the stage 1 breccia.

#### ***Stage 2 chaotic matrix-supported breccia:***

The stage 2 breccia is a domain of intense brecciation and kaolinite-muscovite alteration that has cross cut stage 1 (Fig. 10) and has been cross cut by stage 4-C (illite veins and alteration). The stage 2 breccia also cross cuts, and is cross cut by, facies 3B-2 breccias. Stage 2 is characterized by massive, matrix-supported, chaotic, poorly sorted polymict lithic breccia (Table 6; Fig. 12C). Clast shape varies from sub-angular to well-rounded and there is a high proportion of massive matrix that is dominated by rock flour and angular lithic fragments (Fig. 12D). Visible fragments in the matrix have the same composition as clasts, and typically range from medium-sand to granule-sized. The stage 2 breccia is associated with intense kaolinite-muscovite alteration with local pyrite- and quartz-flooding, some of which may also relate to earlier (stage 1) and later (stage 4) alteration events, or in the case of kaolinite, supergene weathering as a result of pyrite oxidation. Kaolinite-muscovite alteration is texturally destructive and affected both clasts and matrix (Fig. 12E). Alteration intensity increases with brecciation intensity and large intervals of drill core from this domain are

unconsolidated. Notably, intense quartz-altered domains occur as unconsolidated quartz sand. Domains of the stage 2 breccia correspond with high grade intervals of both Cu and Au (e.g., 181 m @ 1.0 % Cu, 0.3 g/t Au, 173 ppm Mo, including 71 m @ 1.6 % Cu, 0.4 g/t Au, 229 ppm Mo, PRP0711; Hot Chili Ltd, 2013). Mineralization is interpreted to be due to overprinting by stage 3. Chalcopyrite is observed predominately in stage 3B-2 veins with tourmaline (Fig. 12D). Chalcopyrite also occurs as disseminated grains within strongly brecciated zones. Chalcopyrite is commonly replaced by covellite at grain boundaries (Fig. 12F).

*Stage 3 potassic alteration, tourmaline breccias, and main stage mineralization:*

Tourmaline-cemented breccias and associated alteration define the most abundant and widely developed paragenetic stage in the ore zones at the Productora deposit. Most of the Cu-Au-Mo mineralization is associated with the stage 3 hydrothermal breccia complex, with sulfide precipitated as cement along with tourmaline, magnetite, biotite, and other minor phases in varying proportions. Sulfides also occur in syn-brecciation veins and as disseminations in altered clasts. Stage 3 has been subdivided into two sub-stages: stage 3A — K-feldspar alteration and related veins, and stage 3B — tourmaline-cemented breccias and related veins. The tourmaline breccias are further subdivided into five facies based on their dominant cement mineralogy and texture (Table 6; Figs. 9, 10). Boundaries between breccia facies are inferred to be gradational. No cross-cutting relationships were observed between the stage 3 sub-facies, implying that stage 3 was potentially a single brecciation event.

Syn-breccia K-feldspar alteration occurs as rinds around breccia clasts, halos around K-feldspar veins (Fig. 13A), and as domains of intense K-feldspar flooding (Fig. 13B). K-feldspar veinlets and tourmaline veins with K-feldspar selvages (0.5 – >2cm wide) are observed distal (>100 m) to the breccia complex. Stage 3A K-feldspar veinlets were overprinted by stage 3B tourmaline-cemented breccias. K-feldspar alteration intensity ranges from moderate to strong. Where moderate, relict textures of the volcanic protoliths are preserved, including phenocrysts and crystal fragments now replaced by K-feldspar. Where strongly developed, alteration is texturally destructive, causing

complete replacement of the groundmass and obscuring clast boundaries, although K-feldspar phenocrysts are commonly preserved (Figure 13B).

Five facies of stage 3B breccia have been identified across the two sections, with facies 3B-1 and 3B-2 observed on the northern section and 3B-3, 3B-4, and 3B-5 on the southern section (Table 6; Figs. 9, 10). Stage 3B breccias are typically massive, monomict, clast-supported, lithic breccias (Fig. 14A-H). Cement mineralogy and distribution show an upward and outward zonation from tourmaline – magnetite – pyrite - chalcopyrite to tourmaline – pyrite – chalcopyrite. In the south of the deposit, stage 3B assemblages also contain biotite, which has undergone retrograde alteration to chlorite (Fig. 14D). Minor cement components include quartz, molybdenite, uraninite, brannerite, apatite, titanite, and ilmenite. The stage 3B breccias vary upward and outward from chaotic, with local cement-supported domains (Fig. 14E), to jigsaw fit texture (Fig. 14A, B). Clasts are typically sub-angular, poorly–moderately sorted, granule–cobble sized lithic fragments. No clasts containing evidence of porphyry mineralization (e.g., porphyry veins) were observed in the current study. Matrix is limited, typically <10%, and consists of moderately sorted, medium sand–granule size, lithic fragments.

Facies 3B-2 is interpreted to be the distal equivalent of 3B-1 and 3B-4 the distal equivalent of 3B-3 in both upward and outward directions. These interpretations are supported by decreasing proportions of breccia cement and increasing internal clast organization (Table 6). Anhydrite veins are locally observed at depth on the southern study section (Figs. 10, 14F). Observations of friable tourmaline and open spaces in weathered breccia intervals imply that anhydrite cement may have been more widespread prior to dissolution during weathering.

Pyrite commonly occurs as large (80–>250  $\mu\text{m}$ ), equant grains within the breccia cement, typically with abundant inclusions of K-feldspar and quartz, and locally with inclusions of chalcopyrite, and, uncommonly, pyrrhotite. Fine (5–10  $\mu\text{m}$ ) disseminated pyrite is also observed within clasts and cement. Chalcopyrite is typically finer grained than pyrite, although a wide size range is observed (5–200  $\mu\text{m}$ ), and occurs as anhedral grains predominantly in breccia cement. Pyrite and chalcopyrite present mutual overgrowth textures, suggesting that conditions varied between pyrite

and chalcopyrite stability (Fig. 14G). Magnetite occurs as both aggregates of smaller grains (20–100  $\mu\text{m}$ ), commonly associated with chlorite, and in coarser late veins (e.g., facies 3B-5). Its habit varies from anhedral to euhedral and locally contains inclusions of chalcopyrite and pyrite, and in some places has been overgrown by these phases (Fig. 14H). Molybdenite blades and laths occur in association with tourmaline in stage 3B breccia cement, veins, and disseminations in the altered rocks.

#### *Stage 4:*

Stage 4 is divided into several sub-stages, including 4A chlorite veins (Fig. 15A), 4B chalcopyrite – pyrite veinlets, 4C illite veins and alteration, and 4D epidote veins and alteration. Stage 4A and 4B veins cross cut earlier breccias. Stage 4B veins are typically planar, <1–3 mm wide, and occur sparsely and in sheeted arrays. Massive stage 4C illite  $\pm$  pyrite  $\pm$  chlorite-veins, ranging between 5 mm and 5 cm in width, cross cut all earlier alteration stages (Fig 15B). Stage 4D epidote is commonly observed in drill core from the west of section 6,822,215 mN where it occurs in narrow veinlets (<4 mm), stockworks (Fig. 15C), disseminated grains, and feldspar-phenocryst replacements.

#### *Stage 5 calcite veins and breccias:*

Stage 5 calcite cross cuts all earlier assemblages and ranges from hairline veinlets to massive breccia veins. Hairline veinlets are ubiquitous across the deposit, whereas distinctive stage 5 comb-textured veins and calcite-cemented breccias (Fig. 15D) were only observed peripheral to the mineralized breccia complex at depths of >150 m below surface.

#### ***Alice porphyry***

A quartz-vein stockwork is hosted by the Alice granodiorite porphyry. The paragenesis includes early stage quartz - pyrite  $\pm$  chalcopyrite veins that lack internal symmetry (Fig. 16A) and granular quartz-K-feldspar veins (Fig. 16D). Early stage anhydrite veins are also observed locally (Fig. 16B). Planar quartz veins with central seams and variable pyrite, chalcopyrite, and molybdenite contents cross cut the early stage veins (Fig. 16B-D). Late stage pyrite and anhydrite veins cut the earlier veins (Fig. 16E, F). Dark chlorite veins, which locally transition laterally to breccia veins up to

30 cm wide, cross cut earlier veins but are themselves locally cross cut by anhydrite veins (Fig. 16F), which also cross cut pyrite veins. Late stage epidote  $\pm$  chlorite and calcite veins cross cut all other vein types (Fig. 16G).

Potassic alteration is associated with the early stage quartz - pyrite  $\pm$  chalcopyrite veins and planar quartz - pyrite  $\pm$  chalcopyrite  $\pm$  molybdenite veins. Potassic alteration is manifested as biotite  $\pm$  actinolite replacement of hornblende. Quartz - actinolite - chlorite – magnetite alteration locally overprinted the potassic alteration. The margins and deeper parts of the porphyry stock were overprinted by albite  $\pm$  epidote  $\pm$  sericite alteration, which caused local destruction of biotite and chalcopyrite (R. Sillitoe, pers. commun., 2015). Late stage chlorite - muscovite alteration is ubiquitous, and caused replacement of biotite by chlorite and plagioclase by muscovite.

### ***Silica Ridge lithocap***

Lithocaps are defined as lithologically controlled zones of pervasive silicic and advanced argillic alteration with stratigraphically and structurally controlled components, the latter including their subvertical root zones (Sillitoe, 1995; Chang et al., 2011). Remnants of a lithocap crop out on a ridgeline (known as Silica Ridge) immediately above and alongside the Alice porphyry prospect. The lithocap forms resistant high points along the north-striking ridgeline that extends for over 6 km (Fig. 17A). The ridge is disjointed and offset by several faults in the south (Fig. 7). The lithocap consists predominantly of massive, fine-grained, quartz-replaced rocks (Fig. 17B, C). Locally, there is evidence of chaotic, poorly sorted pebble to cobble-sized, quartz-cemented lithic breccias (Fig. 17B). Narrow breccia veins with botryoidal chalcedony cement and open space, and tourmaline-cemented breccias were also observed locally (Fig. 17C). Previous authors have also noted occurrences of the borosilicate dumortierite (Fox, 2000; R. Sillitoe pers. commun., 2015). Directly beneath the lithocap, alunite is exposed on hillsides and in road cuttings, and has also been identified in drill cuttings from holes adjacent to the lithocap. Pyrophyllite and dickite are observed down slope from the alunite and massive quartz, and in drill cuttings from >178 m depth.

### ***Hypogene mineralization***

Copper, Au, and Mo mineralization at Productora is spatially and paragenetically associated with the stage 3 tourmaline-cemented breccia complex (Figs. 18, 19). Chalcopyrite, the principal hypogene Cu-sulfide mineral, predominantly occurs with pyrite as breccia cement and syn-breccia veins (Fig. 14H). Pyrite and chalcopyrite are largely absent from the upper 100 m of the deposit, which is in part due to weathering, and in part to the distribution of breccia facies. Section 6,822,215 mN has high pyrite abundance associated with the stage 2 breccia domain, but pyrite diminishes with depth (Fig. 20A). Pyrite abundance increases with depth on section 6,820,850 mN (Fig. 20C). Covellite and minor chalcocite occur in the upper parts of the sulfide domain, and the lower parts of the weathered zone. Petrographic observations of covellite partially replacing chalcopyrite along grain boundaries provide evidence that covellite is most likely supergene. Estimates of chalcopyrite and pyrite abundances from QXRD combined with whole rock geochemical assays (Escolme et al., 2019) show that the ratio of chalcopyrite to pyrite is much higher on the northern section (py:cpy ~1) compared to the south (py:cpy <0.25; Fig. 20C, D).

Based on observations from the two study sections, the shallower level tourmaline-rich breccia facies, 3B-2 and 3B-4, are typically higher in grade (average 0.46% Cu, 0.1 g/t Au, and 117 ppm Mo) than the deeper-seated, magnetite - tourmaline-cemented breccia facies (3B-1 and 3B-3; average 0.34 % Cu, 0.08 g/t Au, and 110 ppm Mo). The breccia facies observed on the northern section (6,822,215 mN; stage 2, 3B-1 and 3B-2) contain more Mo than those on section 6,820,850 mN. Discrete zones of high grade mineralization are observed within the stage 2 breccia domain (Fig. 18). Although stage 2 was not a mineralizing event, significant mineralization formed where the stage 2 breccia was overprinted by the 3B-2 facies. This ore domain is known as the Habanero ore zone (Hot Chili Ltd, 2013). On average, the Habanero zone has the highest grades of Cu (average 0.8 %, locally up to 5.81 %), Au (average 0.2 g/t, maximum 1.44 g/t), and Mo (average 141 ppm, up to 2340 ppm). Published intercepts from the Habanero ore zone include 72 m @ 0.7 % Cu from 120 m and 102 m @ 1.0 % Cu and 0.2 g/t Au from 124 m (Hot Chili Ltd, 2013; Fig. 18). The high grades are likely to have resulted from the interaction of mineralizing fluids with the stage 2 breccia that was a

favorable site for ore deposition due to high permeability and surface area (e.g., abundant matrix and rock flour; Table 6).

### ***Age of mineralization***

Paragenetic relationships identified in the current study and by previous studies (Fox, 2000; Ray and Dick 2002) established the sequence of brecciation and alteration events detailed in Figure 8. Fox (2000) proposed that the absolute age of the Productora main stage mineralization was  $91.4 \pm 0.2$  to  $90.7 \pm 0.7$  Ma, based on  $^{39}\text{Ar}$ - $^{40}\text{Ar}$  dating of hydrothermal K-feldspar (Table 7). More recently, Re-Os dating of molybdenite yielded an age of  $128.9 \pm 0.6$  Ma (Marquardt et al., 2015; Table 7). During the current study, the absolute timing of mineralization at Productora and the Alice porphyry was further investigated, with additional Re-Os geochronology of molybdenite.

Two drill core samples were dated by Re-Os geochronology methods (see Methods section). Analysis of molybdenite disseminated in K-feldspar altered rhyodacite lapilli tuff from the 3B-3 facies at Productora returned a  $^{187}\text{Re}/^{187}\text{Os}$  age of  $130.1 \pm 0.6$  Ma (Table 8). This is similar to the age by Marquardt et al. (2015; Table 7), the lack of overlap may indicate protracted hydrothermal activity. Molybdenite from a quartz - molybdenite - chalcopyrite - pyrite vein in the Alice porphyry deposit returned a  $^{187}\text{Re}/^{187}\text{Os}$  age of  $124.1 \pm 0.6$  Ma (Table 8). These mineralization ages indicate that the Productora breccia complex is similar in age to the Cachiuyito stock ( $129.8 \pm 0.1$  Ma; Fox, 2000) and much older than the Ruta Cinco batholith (96.3–92.2 Ma; Fox, 2000 and this study). Alice porphyry mineralization occurred approximately 3–7 m.y. after the formation of the Productora breccia complex. Uranium-Pb<sub>zircon</sub> dating results for the Alice porphyry intrusion ( $121.1 \pm 2.1$  Ma; this study; Table 3), are similar to the Re-Os ages for the Alice mineralization ( $124.1 \pm 0.6$  Ma, this study; Table 8). The lack of overlap likely reflects some unquantified error introduced in sampling which may only be resolved through additional sampling and analysis. The much younger Ar-Ar age reported by Fox (2000) for Productora hydrothermal K-feldspar ( $90.7 \pm 0.7$  Ma; Table 7) is interpreted to have resulted from thermal resetting during emplacement of the Ruta Cinco granite.

### ***Supergene mineralization***



The depth of sulfide oxidation is variable across the Productora deposit, but typically ranges between 80–100 m. Narrow domains of deeper weathering, to 200–350 m and locally 535 m, occur throughout the deposit and coincide with fault zones. Supergene mineralization predominantly occurs in the south of the deposit, where Cu grades range from 0.2 to >1 %. The northern extent of the deposit has a barren or low grade (<0.2 %Cu) oxidation zone. Supergene mineralogy, determined from logging data and QEMSCAN, predominantly consists of covellite, chalcocite, chrysocolla, limonite, and malachite with variable cuprite/native Cu, Cu-Mn-(Fe)-(Co) wads and pseudomalachite/turquoise. The northern section is dominated by chrysocolla and cuprite. In the south, oxidation appears to have been less extensive, and the proportions of relict chalcopyrite and chalcocite are much higher.

### **Sulfur Isotopes**

Forty-six paragenetically constrained sulfide samples from Productora were analyzed by conventional methods (see Methods). Samples were mainly collected from cross sections 6,822,215 mN (n= 27) and 6,820,850 mN (n = 19), and included several paragenetic stages (Productora stages 1, 3, and 4, and Cachiyuyito system) in order to assess spatial and temporal variation in sulfide isotopic compositions. A total of 25 pyrite and 21 chalcopyrite grains were analyzed.

The  $\delta^{34}\text{S}$  values for pyrite and chalcopyrite from Productora range between -8.5 and +2.2 ‰ relative to the Cañon Diablo Troilite (CDT; Table 9; Fig 21); this range is similar to that reported by Fox (2000; Fig. 21A) and overlaps with the range expected for both porphyry and magmatic-hydrothermal IOCG deposits,  $0 \pm 5\text{‰}$  (Field and Gustafson, 1979; Ohmoto and Rye, 1979; Ohmoto, 1986; Ohmoto and Goldhaber, 1997; Williams et al., 2005; Fig. 22). The  $\delta^{34}\text{S}_{\text{sulfide}}$  values preclude any significant input of sulfur from evaporite- or seawater-sourced fluids, which would have relatively high  $\delta^{34}\text{S}$  (Triassic– Early Cretaceous seawater had  $\delta^{34}\text{S}$  ranging from +14 to +15 ‰; Claypool et al., 1980). Thus, a magmatic sulfur source is inferred, and the broad range of  $\delta^{34}\text{S}_{\text{sulfide}}$  values suggests that the magmatic fluids were oxidized ( $\text{SO}_4^{2-} \rightarrow \text{H}_2\text{S}$ ; e.g., Wilson et al., 2007).

Samples from the Cachiuyito alteration system have low  $\delta^{34}\text{S}$  values (-7.8 to -4.2 ‰) compared to the later alteration assemblages. The Productora stage 1 sample has a  $\delta^{34}\text{S}$  value close to 0 ‰ whereas stage 3 samples return a wide range of values (-8.5 to +1.5 ‰) that show no systematic variation across the stage 3 breccia facies. This suggests that the hydrothermal fluids that generated the stage 1 breccia were not as strongly oxidized as the stage 3 fluids. Stage 4B samples have higher  $\delta^{34}\text{S}$  values (-3.8 to +1.1 ‰) than stage 3 breccia cement, which is the opposite of what would be expected if the sulfides were produced by cooling from a single fluid. This isotopic reversal is therefore interpreted as either evidence of fluid mixing or a later pulse of either a less oxidized fluid or a higher temperature fluid. A pulse of less oxidized fluid is favored because stage 4B has an assemblage of chalcopyrite, pyrite  $\pm$  muscovite, indicating lower temperatures than the K-feldspar-, tourmaline- and magnetite-rich stage 3 assemblages. Stage 4B (-3.8 to +1.1 ‰), 4C (-5.0 to -3.1 ‰), and stage 5 (-6.1 to -4.0 ‰) have increasingly negative  $\delta^{34}\text{S}$  values (Table 9; Fig. 21B), which are consistent with cooling of an oxidized fluid. Within each paragenetic group, chalcopyrite has lower  $\delta^{34}\text{S}$  values than pyrite, and samples from the northern section (6,822,215 mN) typically have lower  $\delta^{34}\text{S}$  values than the southern section (Fig. 21C, D). This shift toward positive  $\delta^{34}\text{S}$  values in the south (Fig. 21) suggests that sulfides were either deposited from a hotter fluid in this area or from one which was less oxidized (i.e., lower  $\text{SO}_4^{2-}/\text{H}_2\text{S}$  ratio). The former supports the interpretation that the roots of the breccia complex are in the south of the deposit.

## **Radiogenic Isotopes**

In this study, Sr isotopes were used to trace the evolution of the hydrothermal fluids involved in mineralization of the Productora breccia complex and, specifically, to determine if connate and/or magmatic fluids were involved. Tourmaline is an ideal mineral for Sr isotope tracer studies of mineralizing fluid at Productora for several reasons: a) tourmaline commonly has high Sr and low Rb contents (Taylor and Slack, 1984; King and Kerrich, 1989; Griffin et al., 1996), b) tourmaline coprecipitated with chalcopyrite, c) tourmaline is relatively resistant to alteration and weathering, and can act as a closed system with respect to Rb-Sr isotope systematics (King and Kerrich, 1989).

The Sr isotopic compositions of eight tourmaline samples from the Productora breccia complex and associated veins were analyzed (see Methods). The initial Sr ratios of tourmaline ( $^{87}\text{Sr}/^{86}\text{Sr}_i$ ) are primitive, ranging between 0.70380 and 0.70432 (Table 10; Fig. 23). The mean value (0.70397), is comparable to the mean ratio for Cretaceous intrusive rocks of northern Chile (0.703976; McNutt et al., 1975; Rogers and Hawkesworth, 1989; Lucassen et al., 2002; Morata and Aguirre, 2003; Girardi, 2014), but is higher than that of the Ruta Cinco batholith (0.7036; McNutt et al. 1975; Fig. 23). No samples from the Cachiyuyito stock were available for analysis in the current study. The initial Sr ratios are consistent with a predominantly mantle-derived source of Sr, either by leaching of mantle-derived igneous rocks or exsolution from mantle-derived magma. There is no evidence for Sr sourced from evaporites, which would have a more radiogenic signature (Richards and Noble, 1998).

## Discussion

### *Breccia genesis*

The Productora breccia complex shows similarities in mineralogy and texture to other Andean mineralized tourmaline-cemented hydrothermal breccias, such as at Cabeza de Vaca and San Pedro de Cachiyuyo (Chile; Sillitoe and Sawkins, 1971). Although a notable point of difference is that while an early sericite alteration event is observed at Productora, the dominant alteration is K-feldspar, which is not common in other Andean tourmaline-cemented breccias. The breccias at Productora formed during several brecciation events with at least two stages of hydraulic fragmentation, stages 1 and 3, and one tectonic-hydrothermal brecciation event (stage 2; Table 11).

The stage 1 breccia has textures consistent with high energy, explosive hydraulic  $\pm$  seismic rupture-driven fragmentation (massive, chaotic, poorly sorted angular clasts; Table 11). Stage 2 is interpreted to be a tectonic breccia generated by seismic rupture-driven fragmentation and attrition during faulting, as evidenced by abundant rock flour and matrix, lack of hydrothermal cement, and rounded and stratified clasts. Clast textures show evidence of multiple brecciation episodes, suggesting local host-fault reactivation. A juxtaposition in host rock lithology from rhyodacite to rhyolite on section 6,822,215 mN supports this interpretation. Stage 3 breccia textures are consistent

with non-explosive hydraulic  $\pm$  seismic rupture-driven fragmentation (minor matrix, clast supported, jigsaw fit). Variability in the texture and clast organization of the stage 3 breccia facies (Tables 6) reflects the interplay of hydraulic fracturing and seismic rupture as a result of hydrostatic pressure exceeding lithostatic load and tensile strength of the rock mass (e.g., Burnham, 1979, 1985). Angular, monomict clasts and clast-supported jigsaw-fit textures indicate little clast transport has occurred. Contact relationships between the stage 3 breccia and its host rocks have not been well established, but the distribution of associated mineralization indicates a downward-tapering, dike-like morphology, ranging from 300 m wide near surface to <100 m at depth (Figs. 3, 4), and a north-northeast strike extent of >2.5 km. The breccia complex extends to depths of >400 m below the present surface. The dike-like geometry of the breccia complex suggests that one or more pre-existing north-northeast striking faults provided a zone of weakness that favored breccia propagation. Hydrothermal fluids brecciated the host rocks, which provided permeability for those fluids to migrate through the rock mass, leading to clast comminution, matrix generation, cementation, and alteration.

#### ***Alteration, veining, and mineralization***

Four types of alteration assemblage are recognized at Productora: phyllic, potassic, argillic, and propylitic (Table 12). In the absence of fluid inclusion studies, experimentally derived phase diagrams based on active geothermal systems and thermodynamic modelling enable paleo-temperatures and pH to be broadly estimated based on the observed mineralogy (Browne, 1978; Hemley et al., 1980; Henley and Ellis, 1983; Hedenquist and Houghton 1987; Reyes 1990; Spear, 1993; Cooke et al., 1996; Losada-Calderon and McPhail, 1996; Masterman, 2003; Seedorff et al., 2005). Stage 1 fluids, which formed the quartz-pyrite-cemented breccia with pervasive muscovite alteration, are inferred to have been weakly acidic and moderate temperature (300°–400°). Stage 3 fluids were more alkaline and higher temperature (400° to >600°C), precipitating K-feldspar, biotite, tourmaline, and magnetite. On cooling, the stage 3 fluids evolved to become weakly acidic and muscovite-stable, as evidenced by 4B (sulfide-muscovite) and 4C veins (illite). Incursion of alkaline fluids is inferred to have formed lower temperature minerals in stages 4A chlorite, 4D epidote, and 5 calcite veins (Table 12). These may have been distal alkaline hydrothermal products of a younger

intrusive complex, e.g., Alice or Ruta Cinco, or a non-magmatic (connate?) fluid overprint. The mineralogy of stages 4 and 5 are consistent with phyllic (stage 4B and 4C) and propylitic assemblages (stage 4A, 4D, and 5; Gustafson and Hunt, 1975).

The mineralogy of the stage 1 breccia (quartz - pyrite-cemented with muscovite alteration) is somewhat at odds with the alteration sequence commonly observed in both porphyry and IOCG systems, where phyllic alteration typically postdates and cross cuts earlier potassic alteration. The stage 1 breccia is interpreted to be the result of a higher energy, explosive brecciation event based on textural evidence (Table 11). The occurrence of an early breccia event with mineralogy indicative of lower temperature and pH fluids provides evidence for multiple discrete hydrothermal events, which may have different magmatic-hydrothermal fluid sources or evolution. This relationship of early quartz – muscovite alteration followed by tourmaline-cemented breccias has been widely recognized in Chilean Cu-bearing tourmaline breccia pipes (Sillitoe and Sawkins, 1971).

The spatial distribution of stage 3 breccia facies and related veins provides evidence for higher temperature fluids in the magnetite-bearing root zone (stage 3B-1 and 3B-3; 425°–500°C; Figs. 9, 10); they migrated upward and outward, cooling and evolving through water-rock interaction to produce K-feldspar - tourmaline  $\pm$  biotite assemblages (stage 3B-2 and 3B-4). Decreasing proportions of breccia cement and increasing internal clast organization, upward and outward, support this interpretation. On section 6,820,850 mN, chalcopyrite content is highest in the 3B-4 breccia facies. Since the root-zone facies defined by the magnetite-bearing stage 3B-3 breccia have lower chalcopyrite contents than the shallower 3B-4 facies, it is likely that temperatures in the deepest part of the breccia complex were too high for chalcopyrite saturation to occur (Cabri, 1973). In contrast, the stage 3B-1 magnetite-bearing facies, on the northern section (6,822,215 mN), has abundant chalcopyrite at similar elevations. There may also have been a temperature gradient along the breccia dike, with higher temperatures in the south toward a progenitor intrusion.

Kaolinite - muscovite - pyrite alteration of the stage 2 breccia (Habanero ore zone) indicates strongly acidic, moderate temperature fluids. The spatial juxtaposition of a strongly acidic, moderate

temperature alteration assemblage (stage 2) against the higher temperature, alkaline assemblage (stage 3; Fig. 9) suggests either that the alteration assemblages were structurally juxtaposed after they formed or that one assemblage overprinted the other. The Habanero ore zone is hosted by the stage 2 tectonic breccia (Table 11), which is associated with a major steeply dipping fault (Fig. 9). Multiple reactivations of the fault are evident from the polyphase breccias. The fault breccias also cross cut stage 3 tourmaline breccias and veins as a result of reactivation. Abrupt changes in lithology are also seen across the fault: the eastern side is dominated by rhyolite lapilli tuff whereas the western side has more mafic rhyodacite lapilli tuff (Fig. 9). This is consistent with oblique dip-slip movement on the northwest oriented faults (J. Beeson, pers. commun., 2012) and, based on this evidence, we suggest that fault displacement led to the juxtaposition of contrasting alteration assemblages. The intense argillic alteration associated with the Habanero ore zone (Stage 2; Table 12) formed from acidic fluids that may have resulted from either a cooling brine, where  $\text{HCl}_{(\text{aq})}$  dissociation was advanced or vapor condensation into groundwater, with disproportionation of contained  $\text{SO}_2$  to  $\text{H}_2\text{SO}_4$  and  $\text{H}_2\text{S}$ , and dissociation of  $\text{HCl}$  and any  $\text{HF}$  (Giggenbach, 1992; Rye, 1993).

Stage 5 veins are characterized by calcite  $\pm$  chalcopryrite and pyrite. They also contain vugs and comb textures consistent with low- or intermediate-sulfidation epithermal conditions (e.g., White and Hedenquist, 1990; Hedenquist et al., 2000). The occurrence of epithermal veins adjacent to and below the tourmaline-cemented breccias indicates that significant exhumation and uplift occurred prior to emplacement of stage 5 veins.

## **Genetic model**

The Cachiuyito tonalite-diorite stock, emplaced  $129.8 \pm 0.1$  Ma (Fox, 2000), is spatially associated with local magnetite-apatite mineralization and temporally associated with the Productora breccia complex (Fig. 24A and B). Cross cutting relationships indicate that magnetite-apatite mineralization observed on the flanks of the Cachiuyito intrusion predate formation of the breccia complex (Fig. 11D). If the age of magnetite-apatite mineralization is assumed to be similar to the age of the Cachiuyito stock, the mineralization age is consistent with older IOA occurrences in the

Mesozoic belt (128 to 102 Ma; Oyarzun et al., 2003). This is noteworthy since no other examples of cross cutting relationships between IOA and porphyry mineralization in the Coastal Cordillera were found in the literature at the time of writing. Existing absolute age data from the region indicate that Mesozoic porphyry-style mineralization is predominantly younger in age than IOA or IOCG, with larger systems restricted to the late Cretaceous (<104 Ma; Richards et al., 2017). New data from this study provide additional evidence that productive porphyry-style systems were active during the Early Cretaceous.

The Productora hydrothermal system produced a sequence of hydrothermal breccias, tectonic breccias, veins, and alteration assemblages that have been separated into five paragenetic stages: stage 1 quartz-pyrite-cemented breccia; stage 2 chaotic matrix-supported breccia; stage 3 tourmaline breccias; stage 4 phyllic and propylitic veins; and stage 5 propylitic veins (Fig. 8 and 24; Table 6). Mineralization is associated with the stage 3 hydrothermal breccia and stage 2 tectonic-hydrothermal breccia (Habanero). The absolute age of Productora stage 3 brecciation and mineralization has been determined by Re-Os on molybdenite to be  $130.1 \pm 0.6$  to  $128.0 \pm 0.6$  Ma (this study; Marquardt et al., 2015). By inference, the age of local magnetite-apatite mineralization is in the region of 129 Ma, this is younger than the Cachiuyuyito stock but older than Productora.

Stage 3 breccia cement mineralogy varies vertically and laterally through the breccia complex. At depth (>200 m), magnetite-bearing assemblages indicate precipitation from high temperature fluids (425°–500°C). Magnetite transitions upward and outward to tourmaline-chalcopyrite dominant assemblages. High grade (>1 % Cu) mineralization formed where stage 3 overprinted the stage 2 tectonic breccia. Breccia textures and mineralogy, as indicators of paleo-temperature, imply a temperature gradient and increased intensity of brecciation to the south, which is suspected to be nearer the root zone of the breccia complex.

The Alice porphyry intruded approximately 3–7 m.y. after emplacement of the Cachiuyuyito stock and Productora breccia complex (Fig. 24C). Mineralization primarily occurs as fine grained, disseminated chalcopyrite and pyrite, plus sulfide stringers and quartz-sulfide veins. Alice porphyry

mineralization is dated at  $124.1 \pm 0.6$  Ma (Re-Os<sub>molybdenite</sub>; Table 8). Remnants of a lithocap, consisting of massive quartz and alunite and pyrophyllite-dickite alteration domains, occur above the Alice porphyry. The lithocap outcrops are disjointed and offset to the southwest (Fig. 2), suggesting that they are remnants of a larger, shallow level domain of advanced argillic and silicic alteration that has mostly been eroded. Absolute timing relationships for the lithocap have not been established, but it is inferred to be coeval with the Alice porphyry.

### ***Genetic classification: porphyry or IOCG?***

Productora is a controversial deposit in terms of ore deposit classification, as it presents features consistent with both the porphyry Cu and IOCG models. Features consistent with the IOCG model include uranium minerals, structural controls, local magnetite-apatite mineralization, large scale sodic-calcic alteration, regional presence of IOCG deposits, and lack of a confirmed progenitor intrusion.

Uranium minerals are observed as accessory phases at Productora, in particular they were observed with breccia cement in stage 3B breccias (Table 6). Uranium minerals are commonly noted in deposits of the IOCG clan, although Andean IOCGs typically contain low U compared to other IOCG deposits (3–5 ppm; Marschik and Fontboté, 2001; Marschik et al., 2000; Hitzman and Valenta, 2005; Williams et al., 2005). Uranium exploration was conducted across the project in the 1980's (Table 1), with a small resource defined, and whole rock U contents from drill core assays at Productora average 17 ppm on the two sections studied (Escolme, 2016). These values are anomalously high with respect to other Andean IOCG deposits and also to porphyry deposits in general. Further investigation is required to fully understand the U deportment and timing at Productora.

There was a strong structural control on the formation of the Productora breccia complex. It was localized along a fault zone in a zone of structural complexity close to the AFS, and has been disrupted by post-mineralization faults. Strong structural controls are a characteristic feature of IOCG deposits, which are typically localized along high- to low-angle faults that are generally splays off



major, crustal-scale faults (Hitzman et al., 1992; Williams et al., 2005). In northern Chile, the AFS was active during arc magmatism and basin formation, and had a strong influence on the distribution of IOCG, magnetite-apatite and Early Cretaceous porphyry mineralization (e.g., Atherton and Aguirre, 1992; Brown et al., 1993; Sillitoe, 2003).

Local magnetite-apatite mineralization occurs at Productora, on the flanks of the Cachiyuyito stock (Fig. 7, 8). A broad spatial and temporal relationship exists between magnetite-apatite and IOCG deposits (Barton and Johnson, 2000). Where deposits are adjacent, a crude zonal relationship has been proposed (e.g., Manto Verde and Manto Ruso; Rieger et al., 2012). Genetic links have also been inferred based on vertical zonation from deep magnetite-apatite to shallow IOCG mineralization (Espinoza et al., 1996; Sillitoe, 2003) and potentially similar mineralizing fluids proposed (Hitzman et al., 1992).

Large scale sodic-calcic alteration occurs in the Productora district. It is spatially associated with the Cachiyuyito stock, and was overprinted by the Productora system (Fox, 2000; Ray and Dick, 2002). Extensive, regional scale, sodic-calcic alteration is a widely recognized, typically early feature of IOCG deposits, whereas in porphyry systems Na-rich alteration is typically smaller in volume, or superimposed and considered to be related to external fluids (Dilles et al., 1995).

IOCG deposits are known to occur in the Mesozoic metallogenic belt of northern Chile, with Candelaria and Mantoverde being the most notable examples, although they are younger than Productora (Candelaria-Punta del Cobre district 116–114 Ma, Marschik et al., 1997; Mantoverde 117–121 Ma; Benavides et al., 2007). The regional temporal and spatial association of IOCG deposits indicates that geodynamic conditions were favorable for their formation. In contrast, porphyry Cu deposits are less common in the Mesozoic metallogenic belts of central and northern Chile.

No progenitor intrusion has been confirmed for the Productora breccia complex, although an association with the Cachiyuyito stock is inferred based on current evidence (geochronology, map relationships, stable and radiogenic isotopes). A major characteristic of the IOCG clan is the absence of intrusions with an intimate genetic relationship to mineralization (Williams et al., 2005).

Features consistent with the porphyry Cu model include the following: tourmaline-cemented breccias, molybdenum, magnetite, acid alteration assemblages, elevated sulfur, no evidence for connate fluids, coeval magmatism and local, albeit younger, porphyry mineralization (Alice).

Tourmaline-rich breccias are widespread in magmatic-hydrothermal systems of the Andes, particularly the porphyry Cu deposits (Sillitoe and Sawkins, 1971; Sillitoe, 1985; Warnaars et al., 1985). Whilst tourmaline is observed in IOCG deposits globally, it typically only occurs as an accessory phase (e.g., Ernest Henry, Williams et al., 2005; Contact Lake Belt, Mumin, 2007). Tornos et al. (2010, 2012) described abundant tourmaline in Andean IOCG deposits; where it occurs as coarse grained breccia cement (e.g., Silivita and Tropezón) or fine grained replacements (e.g., Candelaria and Carola).

Molybdenum is noted as part of the anomalous metal suite associated with IOCG deposits (Williams et al., 2005) but is not economic, whereas porphyry deposits supply half of the world's Mo (Sillitoe, 2010). Molybdenum in porphyry systems is thought to be enriched due to contamination of melts by lower crustal rocks in areas of thickened crust (Stein and Hannah, 1985; Klemm et al., 2008). Thus, high Mo grades at Productora are consistent with derivation from more evolved felsic melts (e.g., Tornos et al., 2010).

Magnetite is common but not abundant in the Productora deposit, typically <2 vol% but locally up to 11 vol% in the magnetite-rich breccia facies (3B-1 and 3B-3; Figs. 9, 10). In Cu-ore zones at Productora, Fe contents, as determined by composite assays (four-acid digest with ICP-AES) of drillcore, typically range between 1 and 8 wt%. The highest measured Fe content on the study sections is 22.5 wt%. Iron concentrations in Cu-rich IOCGs range between 15–25 wt% Fe in Cu ore zones, significantly more than observed at Productora. Accessory magnetite is common in porphyry-related breccias, potassic alteration assemblages (particularly Au-rich porphyries; Sillitoe, 1979), and early veins (Cu-Au porphyries; Sillitoe, 2003). It is typically present in low concentrations, up to a few volume percent at best, but in some Cu-Au porphyries is noted to exceed 10 vol% (e.g., Grasberg; MacDonald and Arnold, 1994).

Acidic alteration assemblages are generally not well developed in IOCG systems owing to their lower sulfur contents and lower sulfidation state. Where acidic alteration occurs, it is typically less voluminous than Na-Ca-K(-Fe) alteration assemblages, and consists of sericite- hematite - quartz assemblages in felsic rocks (Barton, 2014) and has a near absence of sulfides and sulfates (Kreiner, 2011). Argillic and phyllic assemblages at Productora are associated with significant pyrite and no hematite, which is more typical of porphyry-associated advanced argillic assemblages (e.g., Chang et al., 2011). The Silica Ridge lithocap includes domains of advanced argillic alteration with abundant alunite.

Elevated sulfur contents are indicated by the abundance and broad spatial distribution of sulfide minerals (pyrite, chalcopyrite, and molybdenite) and late stage anhydrite veins at Productora. Porphyry deposits are regarded as huge sulfur anomalies, typically with more sulfur than metals (e.g., Williams-Jones and Heinrich, 2005) whereas IOCGs are sulfur-starved, resulting in abundant iron oxides and minor sulfides (e.g., Williams et al., 2005).

No evidence for connate fluid involvement in mineralization was found from the stable and radiogenic isotope studies. Connate fluids are common in IOCG deposits (e.g., Barton and Johnson, 1996, 2000) but have only rarely been reported in porphyry systems (e.g., Bowman et al., 1987; Dilles and Einaudi, 1992). Although magmatic-dominant IOCG end members are recognized (Barton and Johnson, 2004), the influx of non-magmatic, oxidized, saline, and relatively Cu-rich solutions has been proposed by some as critical to IOCG formation (Hitzman et al., 1992, Barton and Johnson 2000; R. Skirrow, pers. commun., 2017).

The Alice porphyry has a spatial and temporal association with the Productora complex. It provides compelling evidence that Early Cretaceous porphyry mineralization affected the district after formation of the Productora breccia complex.

Although a genetic association with a causative intrusion has not been proven, the absolute age of mineralization of Productora is synchronous with emplacement of the Cachiyuyito stock ( $130.1 \pm 0.6$  to  $128.0 \pm 0.6$  Ma; Tables 3, 7 and 8). Based on the absolute ages, spatial association and the

magmatic nature of the mineralizing fluid, determined from stable and radiogenic isotopes, mineralization at Productora is therefore interpreted to be genetically related to the Cachiyuyito stock. All porphyry deposits are magmatic-hydrothermal in origin (e.g., Seedorff et al., 2005; Sillitoe, 2010), whereas IOCGs can be hybrid, or in some cases (e.g., Tennant Creek, Australia) produced entirely by non-magmatic saline fluids (e.g., Wedekind, 1990).

## Conclusions

The Productora Cu-Au-Mo deposit formed as a result of a series of magmatic-hydrothermal brecciation events associated with intrusion of a deep seated, magmatic-hydrothermal complex (Fig. 24). Mineralizing fluids, and by inference the metals, were predominantly sourced from a crystallizing intrusive complex. Previous authors have interpreted Productora to be a magnetite-dominant IOCG deposit similar to Candelaria, which also has significant sulfide mineralization associated with potassic alteration (Fox, 2000). Based on the available evidence, Productora is considered here to show stronger affinities with porphyry rather than IOCG deposits. The most compelling evidence toward this conclusion includes the tourmaline-dominant mineralogy, high Mo content, low magnetite (relative to IOCGs), and high sulfur content — evidenced by acidic alteration assemblages and abundant sulfide minerals. A magmatic-hydrothermal origin is consistent with the porphyry model. However, the high uranium content observed at Productora is atypical for the porphyry model and requires further investigation. The absolute age of mineralization at Productora ( $130.1 \pm 0.6$  to  $128.0 \pm 0.6$  Ma; this study; Marquardt et al., 2015) overlaps with both the younger IOCG belt (130-110 Ma; Sillitoe, 2003) and the Pacific Porphyry Cu-belt (132-97 Ma; Maksiyev et al. 2007).

Current IOCG literature presents a plethora of characteristic features and environments of formation that promote confusion and ambiguity. Fundamental similarities in the genetic mechanisms of porphyry-related magmatic-hydrothermal breccias and magmatic end-member IOCG deposits results in considerable overlap between these models and deposit classes. For deposits such as Productora that present a wide range of defining features that may correspond to both deposit models, classification is challenging and requires a holistic approach.

## **Acknowledgments**

We thank Hot Chili Ltd for their financial, technical, and logistical support during this study, particularly Melanie Leighton, Samantha Kemp, and Lachlan MacDonald. Thanks are also extended to all those who assisted with field work, including Bruce Hunter, Cristian Vasquez, Antonio Muñoz Algobia, Ana Centeno, Pablo Torres, and Andrea Aravena. This research benefited greatly from the insights of Warren Potma, John Beeson, and Scott Halley, and from Mark Barton and Richard Sillitoe's comments. Thanks go to Christine Cook for undertaking the sulfur isotope analyses, and to Garry Davidson for his insights regarding their interpretation, and to Jay Thompson for undertaking U-Pb geochronology analysis. Sebastian Meffre, Jocelyn McPhie, Joshua Phillips, Ayesha Ahmed and Evan Orovan are thanked for their enlightening discussions and advice. Additional funding for this research was gratefully received from Commonwealth Scientific and Industrial Research Organisation, Society of Economic Geologists, and Australian Institute of Mining and Metallurgy. This research was supported by the ARC Research Hub for Transforming the Mining Value Chain (project number IH130200004).

## References

- Atherton, M.P., and Aguirre, L., 1992, Thermal and geotectonic setting of Cretaceous volcanic rocks near Ica, Peru, in relation to Andean crustal thinning: *Journal of South American Earth Sciences*, v. 5, p. 47–69.
- Barazangi, M., and Isacks, B.L., 1979, Subduction of the Nazca Plate beneath Peru; evidence from spatial distribution of earthquakes: *Geophysical Journal of the Royal Astronomical Society*, v. 57, p. 537–555.
- Barra, F., Reich, M., Selby, D., Rojas, P., Simon, A., Salazar, E. and Palma, G., 2017, Unraveling the origin of the Andean IOCG clan: A Re-Os isotope approach: *Ore Geology Reviews*, v. 81, p. 62–78.
- Barton, M.D., 2014, Iron oxide(-Cu-Au-REE-P-Ag-U-Co) systems: *Treatise on Geochemistry*, Elsevier, v. 13, p. 515–541.
- Barton, M.D., and Johnson, D.A., 1996, Evaporitic-source model for igneous-related Fe oxide-(REE-Cu-Au-U) mineralization: *Geology*, v. 24, p. 259–262.
- Barton, M.D., and Johnson, D.A., 2000, Alternative brine sources for Fe-oxide (-Cu-Au) systems: Implications for hydrothermal alteration and metals, in Porter, T.M., ed., *Hydrothermal iron oxide copper-gold & related deposits: A global perspective*: Adelaide, Porter Geological Publishing, p. 43–60.
- Barton, M.D. and Johnson, D.A., 2004, Footprints of Fe-oxide(-Cu-Au) systems. SEG 2004: Predictive mineral discovery under cover: Centre for Global Metallogeny: Special Publication 33, The University of Western Australia, p. 112–116.
- Benavides, J., Kyser, T.K., Clark, A.H., Oates, C.J., Zamora, R., Tarnovschi, R., and Castillo, B., 2007, The Mantoverde iron oxide-copper-gold district, III Región, Chile: The role of regionally derived, nonmagmatic fluids in chalcopyrite mineralization: *Economic Geology*, v. 102, p. 415–440.
- Berg, K., Breitenkreuz, C., Damm, K.W., Pichowiak, S., and Zeil, W., 1983, The North-Chilean Coast Range—an example for the development of an active continental margin: *Geologische Rundschau*, v. 72, p. 715–731.
- Blackwell, J.L., 2010, Characteristics and origins of breccias in a volcanic hosted alkalic epithermal gold deposit, Ladolam, Lihir Island, Papua New Guinea: Unpublished PhD thesis, Hobart, Australia, University of Tasmania, 203 p.
- Bowman, J.R., Parry, W.T., Kropp, W.P., and Kruer, S.A., 1987, Chemical and isotopic evolution of hydrothermal solutions at Bingham, Utah: *Economic Geology*, v. 82, p. 395–428.
- Browne, P.R.L., 1978, Hydrothermal alteration in active geothermal fields: *Annual Review of Earth and Planetary Sciences*, v. 6, p. 229–248.
- Brown, M., Díaz, F., and Grocott, J., 1993, Displacement history of the Atacama fault system 25°00 S – 27° 00S, northern Chile: *Geological Society of America Bulletin*, v. 105, p. 1165–1174.
- Burnham, C.W., 1979, Magmas and hydrothermal fluids, in Barnes, H.L., ed., *Geochemistry of Hydrothermal Ore Deposits*: New York, John Wiley, p. 71–136.

- Burnham, C.W., 1985, Energy release in subvolcanic environments; implications for breccia formation, *Economic Geology*, v. 80, p. 1515–1522.
- Cabri, J.L., 1973, New data on phase relations in the Cu-Fe-S system: *Economic Geology*, v. 68, p. 433–454.
- Cembrano, J., González, G., Arancibia, G., Ahumada, I., Olivares, V., and Herrera, V., 2005, Fault zone development and strain partitioning in an extensional strike-slip duplex: A case study from the Mesozoic Atacama fault system, Northern Chile: *Tectonophysics*, v. 400, p. 105–125.
- Chang, Z., Hedenquist, J.W., White, N.C., Cooke, D.R., Roach, M., Deyell, C.L., Garcia, J., Gemmell, J.B., McKnight, S., and Cuison, A.L., 2011, Exploration tools for linked porphyry and epithermal deposits: Example from the Mankayan intrusion-centered Cu-Au district, Luzon, Philippines: *Economic Geology*, v. 106, p. 1365–1398.
- Charrier, R., Pinto, L., and Rodríguez, M.P., 2007, Tectonostratigraphic evolution of the Andean Orogen in Chile, in Moreno, T., and Gibbons, W., eds., *The Geology of Chile*: London, The Geological Society, p. 21–114.
- Chen, H., 2010, Mesozoic IOCG mineralisation in the Central Andes: An updated review, in Porter, T.M., ed., *Hydrothermal iron oxide copper-gold and related deposits; a global perspective*: Adelaide, PGC Publishing, p. 259-272.
- Claypool, G.E., Holser, W.T., Kaplan, I.R., Sakai, H., and Zak, I., 1980, The age curves of sulfur and oxygen isotopes in marine sulfate and their mutual interpretation: *Chemical Geology*, v. 28, p. 199–260.
- Coira, B., Davidson, J., Mpodozis, C., and Ramos, V., 1982, Tectonic and magmatic evolution of the Andes of northern Argentina and Chile: *Earth Science Reviews*, v. 18, p. 303–332.
- Cooke, D.R., and McPhail, D., 1996, Telluride mineralisation in low sulfidation epithermal veins—contributions of magmatic volatiles: *Australian Geological Convention*, 13th, Canberra, Australia, 1996, p. 96.
- Cooke, D.R., Deyell, C.L., Waters, P.J., Gonzales, R.I., and Zaw, K., 2011, Evidence for magmatic-hydrothermal fluids and ore-forming processes in epithermal and porphyry deposits of the Baguio district, Philippines: *Economic Geology* v. 106, p. 1399-1424.
- Corbett, G.J., and Leach, T.M., 1998, Southwest Pacific rim gold-copper systems: Structure, alteration, and mineralization: *Society of Economic Geologists Special Publication No. 6*, p. 236.
- Dallmeyer, R.D., Brown, M., Grocott, J., Taylor, G.K., and Treloar, P.J., 1996, Mesozoic magmatic and tectonic events within the Andean plate boundary zone, 26°–27°30'S, North Chile: Constraints from mineral ages: *Geology*, v. 104, p. 19–40.
- Davies, A.G.S., Cooke, D.R., Gemmell, J.B., and Simpson, K.A., 2008a, Diatreme breccias at the Kelian gold mine, Kalimantan, Indonesia: Precursors to epithermal gold mineralization: *Economic Geology*, v. 103, p. 689–716.
- Davies, A.G.S., Cooke, D.R., and Gemmell, J.B., 2008b, Hydrothermal breccias and veins at the Kelian gold mine, Kalimantan, Indonesia: Genesis of a large epithermal gold deposit: *Economic Geology*, v. 103, p. 717-757.

- de Haller, A., and Fontboté, L., 2009, The Raúl-Condestable iron oxide copper-gold deposit, central coast of Peru: Ore and related hydrothermal alteration, sulfur isotopes, and thermodynamic constraints: *Economic Geology*, v. 104, p. 365–384.
- de Haller, A., Zúñiga, A., Corfu, F., and Fontboté, L., 2002, The iron oxide-Cu-Au deposit of Raúl-Condestable: Mala, Lima, Peru [abs.]: *Congreso Geológico Peruano*, 11th, Resúmenes, 2002, p. 80.
- DePaolo, D.J., and Wasserburg, G.J., 1976, Nd isotopic variations and petrogenetic models: *Geophysical Research Letters*, v. 3, p. 249–252.
- Dilles, J. H., and Einaudi, M. T., 1992, Wall-rock alteration and hydrothermal flow paths about the Ann-Mason porphyry copper-deposit, Nevada – a 6-km vertical reconstruction: *Economic Geology*, v. 87, p. 1963–2001.
- Dilles, J.H., Farmer, G.L., and Field, C.W., 1995, Sodium-calcium alteration by non-magmatic saline fluids in porphyry copper deposits: Results from Yerington, Nevada: *Mineralogical Association of Canada Short Course*, v. 23, p. 309–338.
- Escolme, A., 2016, *Geology, geochemistry and geometallurgy of the Productora Cu-Au-Mo deposit, Chile*: Unpublished Ph.D. thesis, Hobart, Tasmania, University of Tasmania, 313 p.
- Escolme, A., Berry, R.F., Hunt, J., Halley, S., Potma, W., 2019, Predictive Models of Mineralogy from Whole-Rock Assay Data: Case Study from the Productora Cu-Au-Mo Deposit, Chile: *Economic Geology*, v. 114, p. 1513–1542.
- Espinoza Reyes, S., Veliz, G.H., Esquivel L.J., Arias Farias, J., and Moraga, B.A., 1996, The cupriferous province of the Coastal Range, northern Chile, in Camus, F., Sillitoe, R.M., and Petersen, R., eds., *Andean Copper Deposits: New discoveries, mineralization styles and metallogeny*: Society of Economic Geologists Special Publication No. 5, p. 19–32.
- Faure, G., and Powell, J. L., 1972, *Strontium isotope geology*: Berlin, Springer-Verlag, 189 p.
- Field, C., and Gustafson, L., 1976, Sulfur isotopes in the porphyry copper deposit at El Salvador, Chile: *Economic Geology*, v. 71, p. 1533–1548.
- Fox, K.A., 2000, *Fe-Oxide (Cu-U-Au-REE) Mineralisation and alteration at the Productora prospect*: unpublished PhD thesis, Colorado School of Mines, p. 114.
- Giggenbach, W.F., 1992, Magma degassing and mineral deposition in hydrothermal systems along convergent plate boundaries: *Economic Geology*, v. 87, p. 1927–1944.
- Girardi, J. D., 2014, *Comparison of Mesozoic magmatic evolution and iron oxide (-copper-gold) ('IOCG') mineralization, Central Andes and western North America*: Unpublished Ph.D. thesis, The University of Arizona, p. 364.
- Griffin, W.L., Slack, J.F., Ramsden, A. R., Win, T.T., and Ryan, C.G., 1996, Trace elements in tourmalines from massive sulfides deposits and tourmalinites; geochemical controls and exploration applications: *Economic Geology*, v. 91, p. 657–675.
- Grocott, J., and Taylor, G.K., 2002, Magmatic arc fault systems, deformation partitioning and emplacement of granitic complexes in the Coastal Cordillera, north Chilean Andes (25°30'S to 27°00'S): *Journal of the Geological Society [London]*, v. 159, p. 425–442.



- Grocott, J., Brown, M., Dallmeyer, R.D., Taylor, G.K., and Treloar, P.J., 1994, Mechanisms of continental growth in extensional arcs: An example from the Andean plate-boundary zone: *Geology*, v. 22, p. 391–394.
- Gustafson, L.B., and Hunt, J.P., 1975, The porphyry copper deposit at El Salvador, Chile: *Economic Geology*, v. 70, p. 857–912.
- Hedenquist, J.W., and Houghton, B.F., 1987, Epithermal gold mineralisation and its volcanic environments: *Earth Resources Foundation, University of Sydney*, p. 422.
- Hedenquist, J.W., Arribas, R., and Gonzalez-Urien, E., 2000, Exploration for epithermal gold deposits: *Reviews in Economic Geology*, v. 13, p. 45–77.
- Hemley, J.J., Montoya, J.W., Marinenko, J.W., and Luce, R.W., 1980, Equilibria in the system  $\text{Al}_2\text{O}_3\text{-SiO}_2\text{-H}_2\text{O}$  and some general implications for alteration/mineralization processes: *Economic Geology*, v. 75, p. 210–228.
- Henley, R.W., and Ellis, A.J., 1983, Geothermal systems ancient and modern: a geochemical review: *Earth-Science Reviews*, v. 19, p. 1–50.
- Henríquez, F., Naslund, H.R., Nyström, J.O., Vivallo, W., Aguirre, R., Dobbs, F.M., and Lledo, H., 2003, New field evidence bearing on the origin of the El Laco magnetite deposit, northern Chile—a discussion: *Economic Geology*, v. 98, p. 1497–1500.
- Hervé, M., 1987, Movimiento sinistral en el Cretácico Inferior de la Zona de Falla de Atacama al Norte de Paposo (24°S), Chile: *Revista Geológica de Chile*, no. 31, p. 37–42.
- Hitzman, M.W., and Valenta, R.K., 2005, Uranium in iron oxide-copper-gold (IOCG) systems: *Economic Geology*, v. 100, p. 1657–1661.
- Hitzman, M.W., Oreskes, N., and Einaudi, M.T., 1992, Geological characteristics and tectonic setting of Proterozoic iron oxide (Cu-U-Au-REE) deposits: *Precambrian Research*, v. 58, p. 241–287.
- Hopper, D., and Correa, A., 2000, The Panulcillo and Teresa de Colmo copper deposits: Two contrasting examples of Fe-ox-Cu-Au mineralisation from the Coastal Cordillera of Chile, in Porter, T. M., ed., *Hydrothermal iron oxide copper-gold and related deposits: A global perspective*, 1: Adelaide, PGC Publishing, p. 177–189.
- Horstwood, M.S., Košler, J., Gehrels, G., Jackson, S.E., McLean, N.M., Paton, C., Pearson, N.J., Sircombe, K., Sylvester, P., Vermeesch, P. and Bowring, J.F., 2016, Community-derived standards for LA-ICP-MS U-(Th-) Pb geochronology—Uncertainty propagation, age interpretation and data reporting: *Geostandards and Geoanalytical Research*, v. 40, p. 311–332.
- Hot Chili Ltd, 2013, Quarterley report: Period ending September 30th 2013, Hot Chili Ltd, Perth.
- Hot Chili Ltd, 2016, ASX announcement Wednesday 2nd March 2016: Hot Chili delivers PFS and near doubles reserves at Productora, Hot Chili Ltd, Perth.
- Hot Chili Ltd, 2017, ASX announcement Thursday 27th April 2017: First drill results confirm Alice extensions at Productora, Hot Chili Ltd, Perth.

- King, R.W., and Kerrich, R.W., 1989, Strontium isotope compositions of tourmaline from lode gold deposits of the Archean Abitibi Greenstone belt (Ontario-Quebec, Canada): Implications for source reservoirs: *Chemical Geology: Isotope Geoscience section*, v. 79, p. 225–240.
- Klemm, L. M., Pettke, T., and Heinrich, C. A., 2008, Fluid and source magma evolution of the Questa porphyry Mo deposit, New Mexico, USA: *Mineralium Deposita*, v. 43, p. 533.
- Knipping, J.L., Bilenker, L.D., Simon, A.C., Reich, M., Barra, F., Deditius, A.P., Lundstrom, C., Bindeman, I., and Munizaga, R., 2015a, Giant Kirunatype deposits form by efficient flotation of magmatic magnetite suspensions: *Geology*, v. 43, p. 591–594.
- Knipping, J.L., Bilenker, L., Simon, A.C., Reich, M., Barra, R., Deditius, A., Wälle, M., Heinrich, C.A., Holtz, F., and Munizaga, R., 2015b, Trace elements in magnetite from massive iron oxide-apatite deposits indicate a combined formation by igneous and magmatic-hydrothermal processes: *Geochimica et Cosmochimica Acta*, v. 171, p. 15–38.
- Kreiner, D., 2011, Epithermal style iron oxide(–Cu–Au) (=IOCG) vein systems and related alteration: Unpublished PhD thesis, Tuscon, Arizona, University of Arizona, p. 659.
- Lieben, F., Moritz, R., and Fontboté, L., 2000, Mineralogy, geochemistry, and age constraints on the Zn-Pb skarn deposit of Maria Cristina, Quebrada Galena, Northern Chile: *Economic Geology*, v. 95, p. 1185–1196.
- Losada-Calderón, A., McPhail, D., Camus, F., Sillitoe, R., and Petersen, R., 1996, Porphyry and high sulfidation epithermal mineralization in the Nevados del Famatina mining district, Argentina, Andean copper deposits: new discoveries, mineralization, styles and metallogeny, *Society Economic Geology Special Publication No. 5*, p. 91–118.
- Lucassen, F., and Thirlwall, M.F., 1998, Sm-Nd ages of mafic rocks from the Coastal Cordillera at 24 degrees S, northern Chile: *Geologische Rundschau*, v. 86, p. 767–774.
- Lucassen, F., Escayola, M., Romer, R.L., Viramonte, J., 2002, Isotopic composition of Late Mesozoic basic and ultrabasic rocks from the Andes (23–32 degrees S) - Implications for the Andean mantle: *Contributions to Mineralogy and Petrology*, v. 143, p. 336–349.
- Maas, R., Grew, E.S., Carson, C.J., 2015, Isotopic constraints (Pb, Rb-Sr, Sm-Nd) on the sources of Early Cambrian pegmatites with boron and beryllium minerals in the Larseman Hills, Prydz Bay, Antarctica: *The Canadian Mineralogist*, v. 53, p. 249-272.
- MacDonald, G.D., and Arnold, L.C., 1994, Geological and geochemical zoning of the Grasberg Igneous Complex, Irian Jaya, Indonesia: *Journal of Geochemical Exploration*, v. 50, p. 143–178.
- Maksaev, V., Townley, B., Palacios, C., and Camus, F., 2007, Metallic ore deposits, in Moreno, T., and Gibbons, W., eds., *The Geology of Chile: The Geological Society, London*, p. 179–199.
- Markey, R., Stein, H.J., Hannah, J.L., Selby, D., and Creaser, R.A., 2007, Standardizing Re-Os geochronology: A new molybdenite Reference Material (Henderson, USA) and the stoichiometry of Os salts: *Chemical Geology*, v. 244, p. 74-87.
- Marquardt, M., Cembrano, J., Bissig, T., and Vásquez, C., 2015, Mid Cretaceous Cu-Au (Mo) mineralization in the Vallenar district: new Re-Os age constraints from Productora deposit, northern Chile, XIV Congreso Geológico Chileno: *La Serena, Sociedad Geologica de Chile*, p. 421–424.

- Marschik, R., and Fontboté, L., 1996, Copper(-iron) mineralization and superposition of alteration events in the Punta del Cobre Belt, northern Chile: Society of Economic Geologists Special Publication No. 5, p. 171–190.
- Marschik, R., and Fontboté, L., 2001, The Candelaria-Punta del Cobre iron oxide Cu-Au(-Zn-Ag) deposits, Chile: Economic Geology, v. 96, p. 1799–1826.
- Marschik, R., Singer, B.S., Munizaga, F., Tassinari, C., Moritz, R., and Fontboté, L., 1997, Age of Cu(-Fe)-Au mineralization and thermal evolution of the Punta del Cobre district, Chile: Mineralium Deposita, v. 32, p. 531–546.
- Marschik, R., Leveille, R., and Martin, W., 2000, La Candelaria and the Punta del Cobre district, Chile: Early Cretaceous iron oxide Cu-Au(-Zn-Ag) mineralization, in Porter, T. M., ed., Hydrothermal iron oxide copper-gold and related deposits: A global perspective, 1: Adelaide, PGC Publishing, p. 163–176.
- Naslund, H.R., Henriquez, F., Nystrom, J.O., Vivallo, W., and Dobbs, F.M., 2002, Magmatic iron ores and associated mineralisation; examples from the Chilean High Andes and Coastal Cordillera, in Porter, T.M., ed., Hydrothermal iron oxide copper-gold and related deposits; a global perspective, 2: Adelaide, PGC Publishing, p. 207–226.
- Masterman, G., 2003, Structural and geochemical evolution of the Rosario Cu-Mo porphyry deposit and related Cu-Ag veins, Collahuasi district, northern Chile: Unpublished PhD thesis, Hobart, Australia, University of Tasmania, p. 253.
- McNutt, R.H., Crocket, J.H., Clark, A.H., Caelles, J.C., Farrar, E., Haynes, S.J., and Zentilli, M., 1975, Initial  $^{87}\text{Sr}/^{86}\text{Sr}$  ratios of plutonic and volcanic rocks of the Central Andes between latitudes 26° and 29° south: Earth and Planetary Science Letters, v. 27, p. 305–313.
- McPhie, J., Doyle, M., and Allen, R., 1993, Volcanic textures: a guide to the interpretation of textures in volcanic rocks: Hobart, Centre of Excellence in Ore Deposits, University of Tasmania, 198 p.
- Ménard, J.J., 1995, Relationship between altered pyroxene diorite and the magnetite mineralization in the Chilean iron belt, with emphasis on the El Algarrobo iron deposits (Atacama region, Chile): Mineralium Deposita, v. 30, p. 268–274.
- Morata, D., and Aguirre, L., 2003, Extensional Lower Cretaceous volcanism in the Coastal Range (29°20'–30°S), Chile: geochemistry and petrogenesis: Journal of South American Earth Sciences, v. 16, p. 459–476.
- Morata, D., Feraud, G., Aguirre, L., Arancibia, G., Belmar, M., Morales, S., and Carrillo, J., 2008, Geochronology of the Lower Cretaceous volcanism from the Coastal Range (29°20'–30°S), Chile: Revista Geológica de Chile, v. 35, p. 123–145.
- Moscoso, R., Nasi, C., and Salinas, P., 1982, Hojo Vallenar y parte norte de La Serena, Regiones de Atacama y Coquimbo, Carta Geológica de Chile, Servicio Nacional de Geología y Minería (Chile), No. 55, p. 1–100.
- Mpodozis, C., and Allmendinger, R.W., 1993, Extensional tectonics, Cretaceous Andes, northern Chile (27 degrees S): Geological Society of America Bulletin, v. 105, p. 1462–1477.

- Mpodozis, C., and Ramos, V.A., 1990, The Andes of Chile and Argentina: Circum-Pacific Council for Energy and Mineral Resources Earth Science Series, v. 11, p. 59–90.
- Mumin, A.H., Corriveau, L., Somarin, A.K., and Ootes, L., 2007, Iron oxide copper-gold-type polymetallic mineralization in the Contact Lake Belt, Great Bear Magmatic Zone, Northwest Territories, Canada: *Exploration and Mining Geology*, v. 16, p. 187–208.
- Naslund, H.R., Henríquez, F., Nyström, J.O., Vivallo, W., and Dobbs, F.M., 2002, Magmatic iron ores and associated mineralization: Examples from the Chilean high Andes and coastal Cordillera, in Porter, T.M., ed., *Hydrothermal iron oxide copper-gold and related deposits: A global perspective*: Adelaide, PGC Publishing, v. 2, p. 207–226.
- Nyström, J.O., and Henríquez, F., 1994, Magmatic features of iron ores of the Kiruna type in Chile and Sweden: Ore textures and magnetite geochemistry: *Economic Geology*, v. 89, p. 820–839.
- Ohmoto, H., 1972, Systematics of sulfur and carbon isotopes in hydrothermal ore deposits: *Economic Geology*, v. 67, p. 551–578.
- Ohmoto, H., 1986, Stable isotope geochemistry of ore deposits: *Reviews in Mineralogy and Geochemistry*, v. 16, p. 491–559.
- Ohmoto, H., and Goldharber, M.B., 1997, Sulfur and carbon isotopes, in Barnes, H.L., ed., *Geochemistry of hydrothermal ore deposits*, 3rd ed.: New York, Wiley, p. 517–611.
- Ohmoto, H., and Rye, R.O., 1979, Isotopes of sulfur and carbon, in Barnes, H.L., ed., *Geochemistry of hydrothermal ore deposits*, 2nd ed.: New York, Wiley, p. 509–567.
- Oliveros, V., Féraud, G., Aguirre, L., Fornari, M., and Morata, D., 2006, The early Andean magmatic province (EAMP):  $^{40}\text{Ar}/^{39}\text{Ar}$  dating on Mesozoic volcanic and plutonic rocks from the Coastal Cordillera, northern Chile: *Journal of Volcanology and Geothermal Research*, v. 157, p. 311–330.
- Oliveros, V., Morata, D., Aguirre, L., Féraud, G., and Fornari, M., 2007, Jurassic to Early Cretaceous subduction-related magmatism in the Coastal Cordillera of northern Chile ( $18^{\circ}30' - 24^{\circ}\text{S}$ ): geochemistry and petrogenesis: *Revista Geológica de Chile*, v. 34, p. 209–232.
- Parada, M.A., López-Escobar, L., Oliveros, V., Fuentes, F., Morata, D., Calderón, M., Aguirre, L., Féraud, G., Espinoza, F., Moreno, H., Figueroa, O., Bravo, J.M., Vásquez, R.T., and Stern, C.R., 2007, Andean magmatism, in Moreno, T., and Gibbons, W., eds., *The geology of Chile*: London, The Geological Society, p. 115–146.
- Pilger, R.H., 1981, Plate reconstructions, aseismic ridges, and low-angle subduction beneath the Andes: *Geological Society of America Bulletin*, v. 92, p. 448–456.
- Pollard, P.J., 2000, Evidence of a magmatic fluid and metal source for Fe-oxide Cu-Au mineralization, in Porter, T.M., ed., *Hydrothermal iron oxide copper-gold and related deposits: A global perspective*, v. 1: Adelaide, PGC Publishing, p. 27–41.
- Pollard, P.J., 2001, Sodic(-calcic) alteration in Fe-oxide-Cu-Au districts: An origin via unmixing of magmatic  $\text{H}_2\text{O}-\text{CO}_2-\text{NaCl} \pm \text{CaCl}_2-\text{KCl}$  fluids: *Mineralium Deposita*, v. 36, p. 93–100.
- Ramírez, L.E., Palacios, C., Townley, B., Parada, M.A., Sial, A.N., Fernandez-turiel, J.L., Gimeno, D., Garcia-valles, M., and Lehmann, B., 2006, The Mantos Blancos copper deposit: an upper Jurassic

- breccia-style hydrothermal system in the Coastal Range of Northern Chile: *Mineralium Deposita*, v. 41, p. 246–258.
- Ramirez, L. E., Parada, M. A., Palacios, C., and Wittenbrink, J., 2008, Magmatic evolution of the Mantos Blancos copper deposit, Coastal Range of northern Chile: insight from Sr-Nd isotope, geochemical data and silicate melt inclusions: *Resource Geology*, v. 58, p. 124–142.
- Ramos, V.A., and Folguera, A., 2009, Andean flat-slab subduction through time: Geological Society, London, Special Publications, v. 327, p. 31–54.
- Ramos, V.A., 1999, Plate tectonic setting of the Andean Cordillera: *Episodes*, v. 22, p. 183–190.
- Ray, G.E., and Dick, L.A., 2002, The Productora prospect in north-central Chile: An example of an intrusion-related, Candelaria type Fe-Cu-Au hydrothermal system, in Porter, T.M., ed., *Hydrothermal Iron Oxide, Copper-Gold & Related Deposits: A Global Perspective*, 2: Adelaide, PGC Publishing, p. 131–151.
- Reich, M., Simon, A.C., Deditius, A., Barra, F., Chrysosoulis, S., Lagas, G., Tardani, D., Knipping, J., Bilinker, L., Sánchez-Alfaro, P. and Roberts, M.P., 2016, Trace element signature of pyrite from the Los Colorados iron oxide-apatite (IOA) deposit, Chile: A missing link between Andean IOA and iron oxide copper-gold systems?: *Economic Geology*, v. 111, p. 743–761.
- Reyes, A. G., 1990, Petrology of Philippine geothermal systems and the application of alteration mineralogy to their assessment: *Journal of Volcanology and Geothermal Research*, v. 43, p. 279–309.
- Rhodes, A.L., and Oreskes, N., 1999, Oxygen isotope composition of magnetite deposits at El Laco, Chile: Evidence of formation from isotopically heavy fluids: *Society of Economic Geologists Special Publication 7*, p. 333–351.
- Rhodes, A.L., Oreskes, N., and Sheets, S., 1999, Geology and rare earth element geochemistry of magnetite deposits at El Laco, Chile: *Society of Economic Geologists Special Publication 7*, p. 299–332.
- Richards, J.P., and Mumin, A.H., 2013a, Magmatic-hydrothermal processes within an evolving Earth: Iron oxide-copper-gold and porphyry Cu  $\pm$  Mo  $\pm$  Au deposits: *Geology*, v. 41, p. 767–770.
- Richards, J.P., and Mumin, A.H., 2013b, Lithospheric fertilization and mineralization by arc magmas: Genetic links and secular differences between porphyry copper  $\pm$  molybdenum  $\pm$  gold and magmatic-hydrothermal iron oxide copper-gold deposits: *Society of Economic Geologists Special Publication No. 17*, p. 277–299.
- Richards, J. P., and Noble, S. R., 1998, Application of radiogenic isotope systems to the timing and origin of hydrothermal processes, in Larson, P. B., and Richards, J. P., eds., *Techniques in hydrothermal ore deposits geology*, 10: Boulder, Society of Economic Geologists, Inc., p. 195–233.
- Richards, J. P., López, G. P., Zhu, J.-J., Creaser, R. A., Locock, A. J., and Mumin, A., 2017, Contrasting tectonic settings and sulfur contents of magmas associated with Cretaceous porphyry Cu  $\pm$  Mo  $\pm$  Au and intrusion-related iron oxide Cu-Au deposits in Northern Chile: *Economic Geology*, v. 112, p. 295–318.

- Rieger, A.A., Marschik, R., and Díaz, M., 2012, The evolution of the hydrothermal IOCG system in the Mantoverde district, northern Chile: new evidence from microthermometry and stable isotope geochemistry: *Mineralium Deposita*, v. 47, p. 359–369.
- Ripley, E.M., and Ohmoto, H., 1977, Mineralogic, sulfur isotope, and fluid inclusion studies of the stratabound copper deposits at the Raul Mine, Peru: *Economic Geology*, v. 72, p. 1017–1041.
- Rogers, G., and Hawkesworth, C.J., 1989, A geochemical traverse across the North Chilean Andes: Evidence for crust generation from the mantle wedge: *Earth and Planetary Science Letters*, v. 91, p. 271–285.
- Rye, R.O., 1993, The evolution of magmatic fluids in the epithermal environment; the stable isotope perspective: *Economic Geology*, v. 88, p. 733–752.
- Scheuber, E., and Gonzalez, G., 1999, Tectonics of the Jurassic-Early Cretaceous magmatic arc of the North Chilean Coastal Cordillera (22 degrees –26 degrees S); a story of crustal deformation along a convergent plate boundary: *Tectonics*, v. 18, p. 895–910.
- Scheuber, E., and Reutter, K.-J., 1992, Magmatic arc tectonics in the Central Andes between 21° and 25°S: *Tectonophysics*, v. 205, p. 127–140.
- Seedorff, E., Dilles, J., Proffett, J., Einaudi, M., Zurcher, L., Stavast, W., Johnson, D., and Barton, M., 2005, Porphyry deposits: Characteristics and origin of hypogene features: *Economic Geology 100<sup>th</sup> Anniversary Volume*, p. 251–298.
- Seegerstrom, K., 1960, Erosion and related phenomena at Parícutin in 1957, U.S. Geological Survey Bulletin 1104-A, p. 1–18
- Selby, D., and Creaser, R.A., 2004, Macroscale NTIMS and microscale LA-MC-ICP-MS Re-Os isotopic analysis of molybdenite: Testing spatial restrictions for reliable Re-Os age determinations, and implications for the decoupling of Re and Os within molybdenite: *Geochimica et Cosmochimica Acta*, v. 68, p. 3897–3908.
- Sillitoe, R.H., 1979, Some thoughts on gold-rich porphyry copper deposits: *Mineralium Deposita*, v. 14, p. 161–174.
- Sillitoe, R.H., 1985, Ore-related breccias in volcanoplutonic arcs: *Economic Geology*, v. 80, p. 1467–1514.
- Sillitoe, R. H., 1987, Copper, gold and subduction: a trans-Pacific perspective: *Pacific Rim Congress 87*, Gold Coast, QLD, Australia, 1987, p. 399-103.
- Sillitoe, R., 1995, Exploration of porphyry copper lithocaps: *Proceedings of Pacific Rim Congress*, Auckland, New Zealand, 1995, p. 527–532.
- Sillitoe, R.H., 2003, Iron oxide-copper-gold deposits: An Andean view: *Mineralium Deposita*, v. 38, p. 787–812.
- Sillitoe, R.H., 2010, Porphyry copper systems: *Economic Geology*, v. 105, p. 3–41.
- Sillitoe, R.H., and Burrows, D.R., 2002, New field evidence bearing on the origin of the El Laco magnetite deposit, northern Chile: *Economic Geology*, v. 97, p. 1101–1109.

- Sillitoe, R.H., and Perelló, J., 2005, Andean copper province: Tectonomagmatic settings, deposit types, metallogeny, exploration, and discovery: *Economic Geology* 100<sup>th</sup> Anniversary Volume, p. 845–890.
- Sillitoe, R.H., and Sawkins, F.J., 1971, Geologic, mineralogic and fluid inclusion studies relating to the origin of copper-bearing tourmaline breccia pipes, Chile: *Economic Geology*, v. 66, p. 1028–1041.
- Spear, F.S., 1993, *Metamorphic phase equilibria and pressure-temperature-time paths*: Washington, D.C., Mineralogical Society of America, p. 799.
- Stein H.J., and Hannah J.L., 1985, Movement and origin of ore fluids in Climax-type systems: *Geology*, v. 13, p. 469–474.
- Taylor, B.E., 1987, Stable isotope geochemistry of ore-forming fluids, in Kyser, T.K., ed., *Stable isotope geochemistry of low temperature processes*: Mineralogical Association of Canada Short Course Handbook 13, p. 337–445.
- Taylor, B.E., and Slack, J.F., 1984, Tourmalines from Appalachian-Caledonian massive sulfide deposits; textural, chemical, and isotopic relationships: *Economic Geology*, v. 79, p. 1703–1726.
- Taylor, G.K., Grocott, J., Pope, A., and Randall, D.E., 1998, Mesozoic fault systems, deformation and fault block rotation in the Andean forearc: a crustal scale strike-slip duplex in the Coastal Cordillera of northern Chile: *Tectonophysics*, v. 299, p. 93–109.
- Tornos, F., Wiedenbeck, M., and Velasco, F., 2012, The boron isotope geochemistry of tourmaline-rich alteration in the IOCG systems of northern Chile: Implications for a magmatic-hydrothermal origin: *Mineralium Deposita*, v. 47, p. 483–499.
- Tornos, F., Velasco, F., Barra, F., and Morata, D., 2010, The Tropezón Cu–Mo–(Au) deposit, Northern Chile: The missing link between IOCG and porphyry copper systems?: *Mineralium Deposita*, v. 45, p. 313–321.
- Vergara, M., Levi, B., Nystrom, J.O., and Cancino, A., 1995, Jurassic and Early Cretaceous island arc volcanism, extension, and subsidence in the Coast Range of Central Chile: *Geological Society of America Bulletin*, v. 107, p. 1427–1440.
- Vivallo, W., and Henríquez, F., 1998, Génesis común de los yacimientos estratoligados y vetiformes de cobre del Jurásico Medio a Superior en la Cordillera de la Costa, Región de Antofagasta, Chile: *Revista Geológica de Chile*, v. 25, p. 199–228.
- Warnaars, F.W., Holmgren, D.C., and Barassi, F.S., 1985, Porphyry copper and tourmaline breccias at Los Bronces-Rio Blanco, Chile: *Economic Geology*, v. 80, p. 1544–1565.
- Wedekind, M.R., 1990, *Geology and geochemistry of the Warrego Au-Cu-Bi mine, Tennant Creek, Northern Territory, Australia*: Unpublished PhD thesis, Hobart, Australia, University of Tasmania, p. 324.
- Williams, P.J., Barton, M.D., Johnson, D.A., Fontboté, L., De Haller, A., Mark, G., Oliver, N.H., and Marschik, R., 2005, Iron oxide copper-gold deposits: geology, space-time distribution, and possible modes of origin, *Economic Geology* 100<sup>th</sup> Anniversary Volume, p. 371–405.

Williams-Jones, A.E., and Heinrich, C.A., 2005, Vapor transport of metals and the formation of magmatic-hydrothermal ore deposits: *Economic Geology*, v. 100, p. 1287–1312.

Wilson, A. J., Cooke, D. R., Harper, B. J., and Deyell, C. L., 2007, Sulfur isotopic zonation in the Cadia district, southeastern Australia: exploration significance and implications for the genesis of alkalic porphyry gold–copper deposits: *Mineralium Deposita*, v. 42, p. 465–487.



FIG. 1. Regional map of northern Chile showing the location of Productora in relation to the Atacama Fault System and Mesozoic magnetite-apatite, IOCG and porphyry deposits. Atacama Fault System from Brown et al. 1993, and deposit locations from Naslund et al. (2002), Sillitoe (2003), and Maksaev et al. (2007).

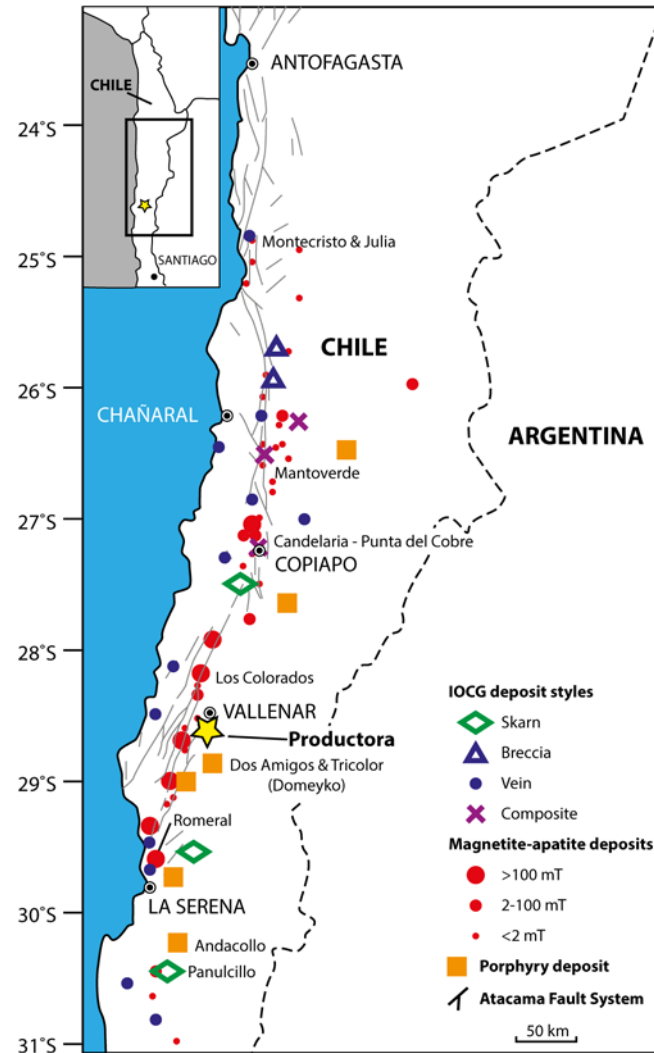


FIG. 2. Map showing local geology and major structures from surface mapping. Also shown are local mineralization occurrences, outline of mineralization (yellow line, defined as Hot Chili Ltd drilling intervals  $>0.1$  %Cu projected to surface), location of two study sections at 6,822,215 mN and 6,820,850 mN, and topography (m). Modified from Ray and Dick (2002), J. Beeson pers. comm., 2012, 2015. 1 = Mariposa, 2 = La Bandera, 3 = La Chulula, 4 = Monseratt, 5 = Remolina, 6 = Productora underground, 7 = Alice, 8 = Santa Inés, 9 = La Negrita, 10 = El Molle, 11 = Zapallo.



FIG. 3. Cross section at 6,822,215 mN showing geology interpreted from graphic core logging, photo logging and immobile element lithogeochemistry. Breccia domains reflect variations in texture and internal clast organisation — protolith textures were largely obscured by alteration and brecciation in these domains. Unusual contact relationships between the rhyodacite lapilli tuff and breccia complex on this section reflect movement on unconstrained faults and the three dimensional shape of the breccia complex.

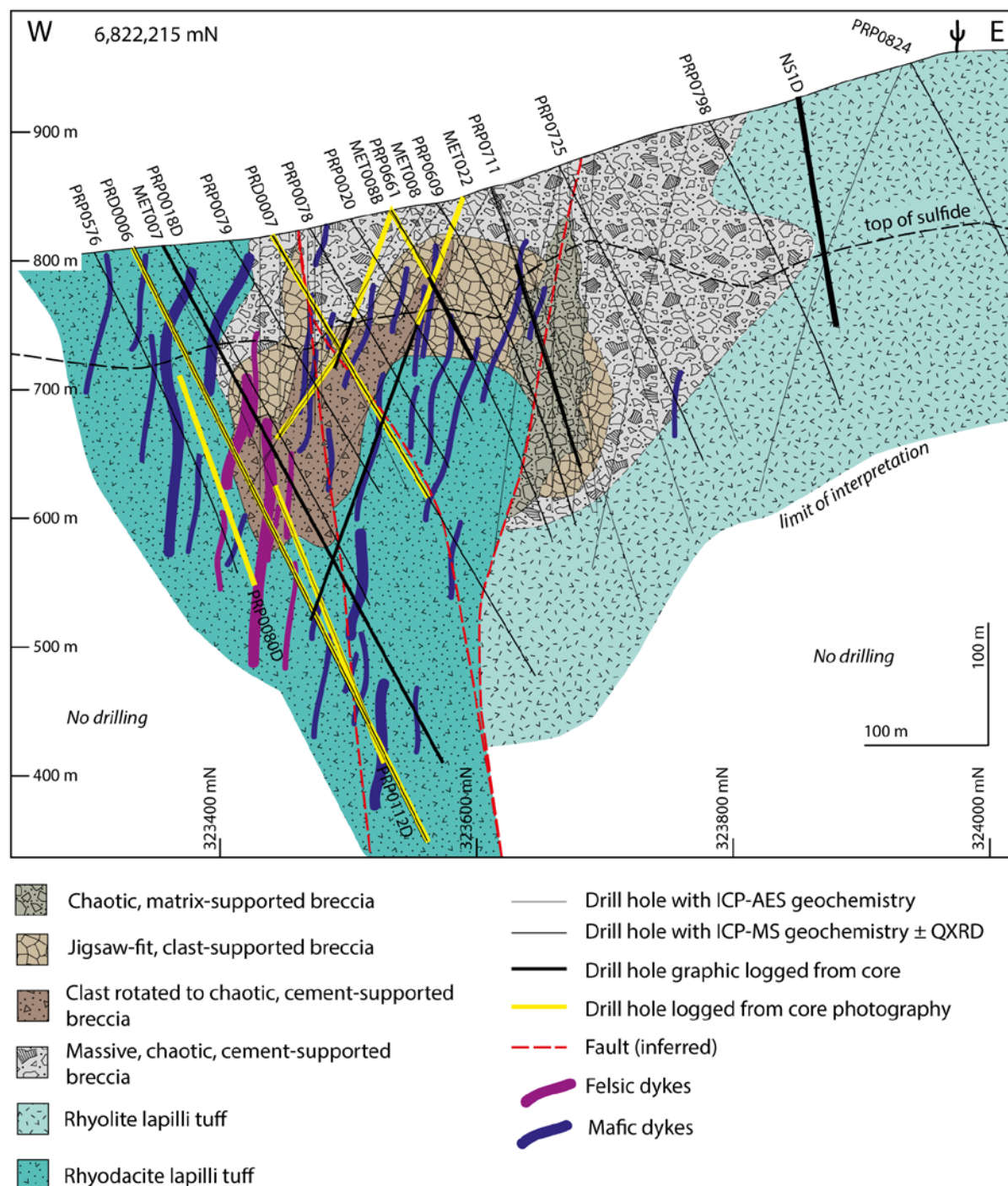


FIG. 4. Cross section at 6,820,850 mN showing geology interpreted from graphic core logging, photo logging and immobile element lithogeochemistry. Breccia domains reflect variations in texture and internal clast organization — protolith textures were largely obscured by alteration and brecciation in these domains.

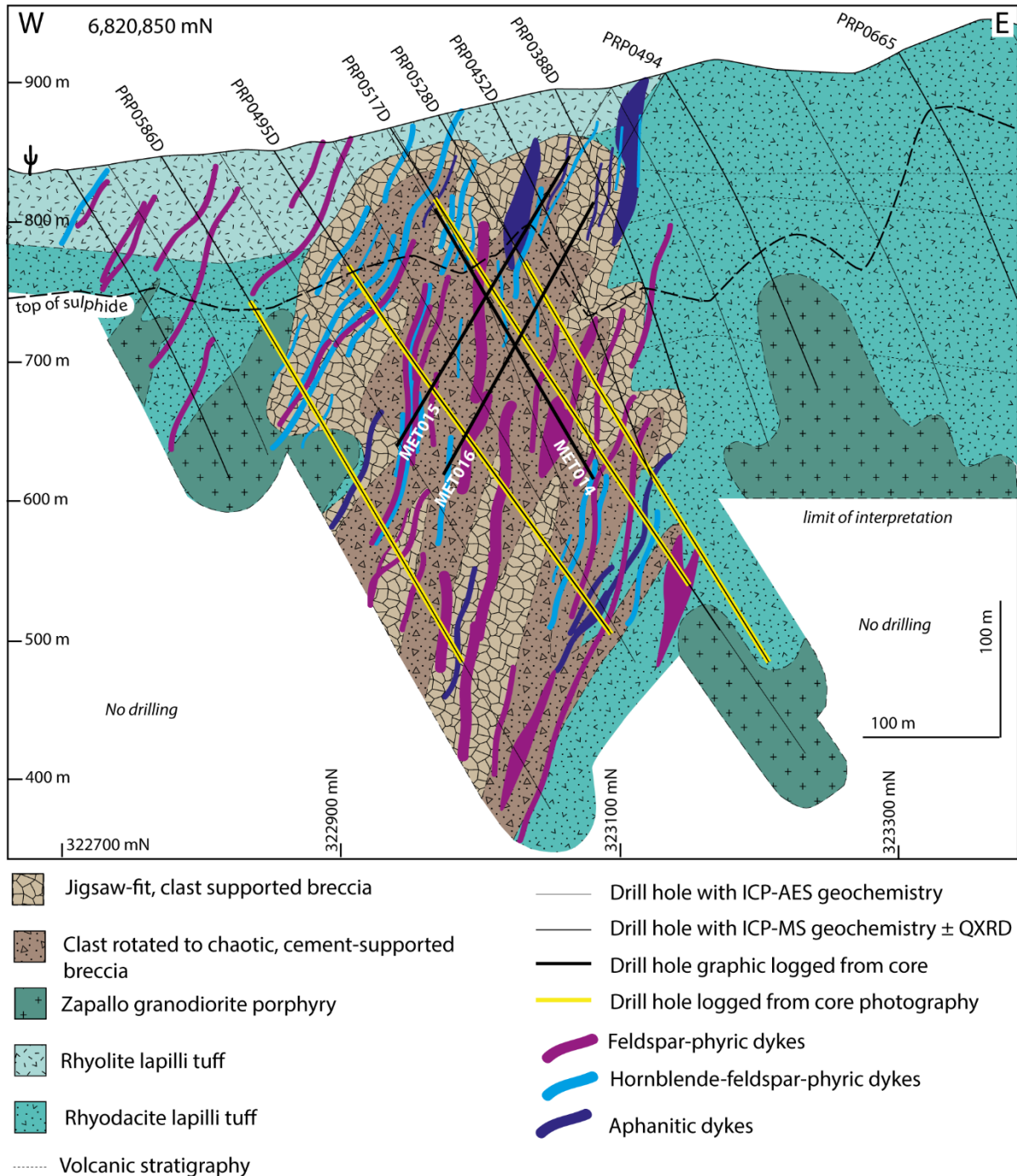




FIG.5. Stratigraphic column for volcanic rocks at the Productora deposit (modified from Fox, 2000) with descriptions for lithologies observed in the current study.

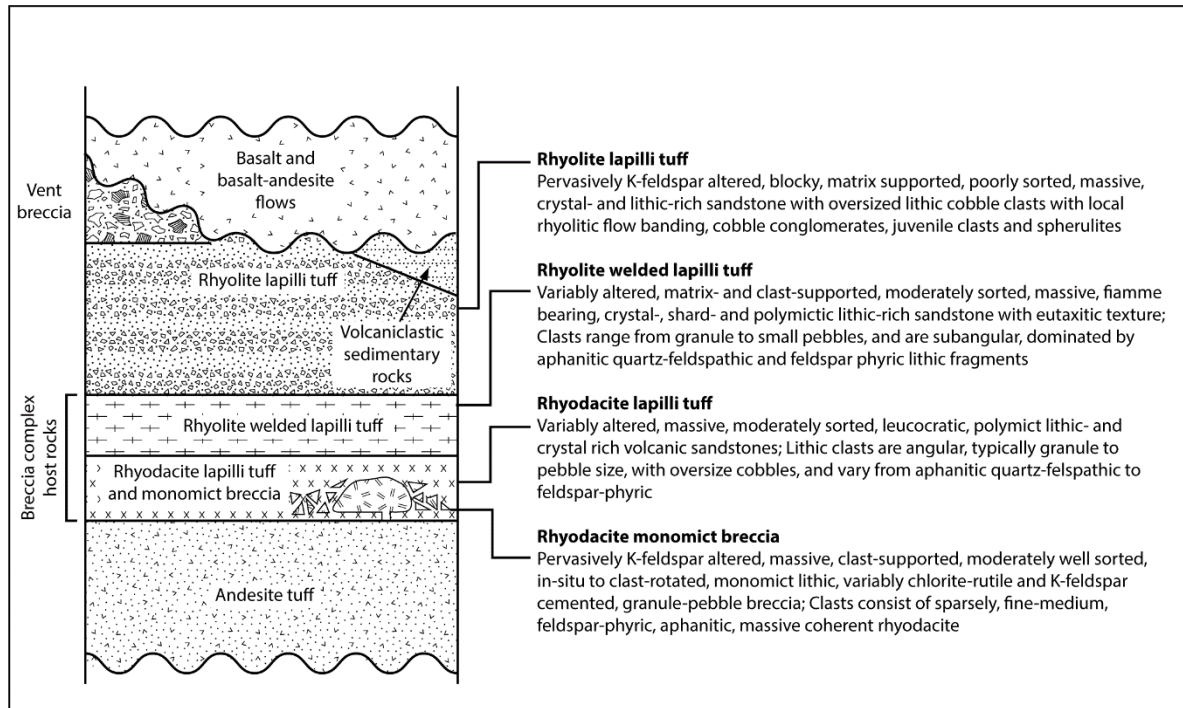


FIG. 6. Representative photos of volcanic and intrusive lithologies. A) Core photo of rhyodacite lapilli tuff showing crystal-poor interbed with polymict lapilli, some with strong K-feldspar alteration, and normal graded bedding (PR14AE047; MET007 376.5 m). B) Plane-polarised transmitted light photo of rhyodacite monomict breccia showing clast with feldspar phenocrysts in aphanitic groundmass (PR14AE021; MET008B 103.90 m). C) Plane-polarised transmitted light photo of welded rhyolite lapilli tuff showing welded groundmass mantling quartz and feldspar crystals (PR14AE143; NS1 143.60 m). D) Hand specimen photo of Ruta Cinco quartz monzodiorite core-phase showing medium grained quartz, feldspar, hornblende and biotite (PR14AE120). E) Core photo of Zapallo medium-grained, granodiorite porphyry with diorite xenolith (PR14AE175, MET016 328.5 m). Sample locations provided in Appendix 1. bt = biotite, hbl = hornblende.

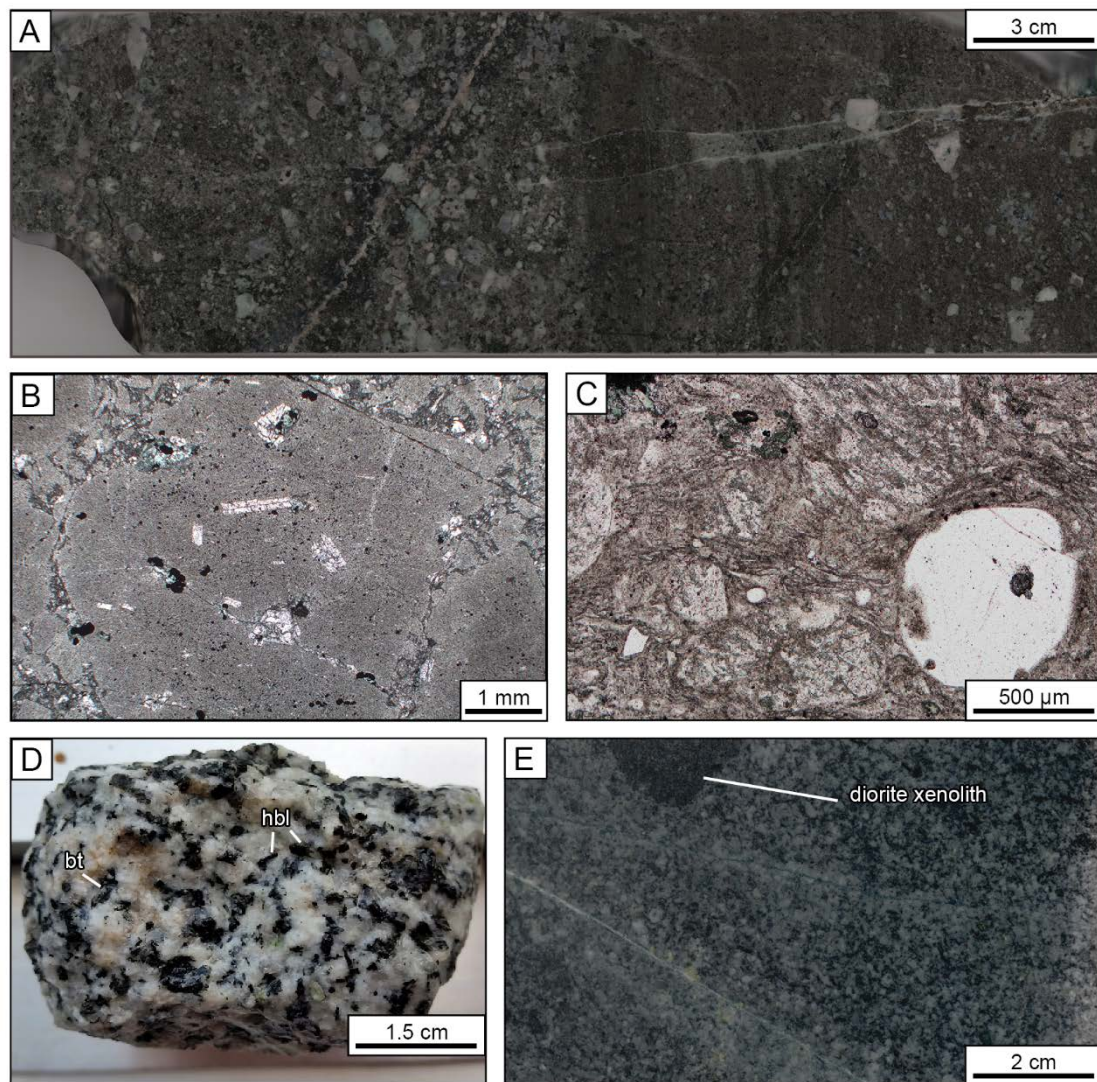


FIG.7. Map showing alteration with local geology and major structures from surface mapping. Also shown are local mineralization occurrences, outline of mineralization (red line, defined as Hot Chili Ltd drilling intervals  $>0.1$  %Cu projected to surface) and location of study section lines 6,822,215 mN and 6,820,850 mN. Modified from Ray and Dick (2002) and J. Beeson pers. commun., 2012, 2015.

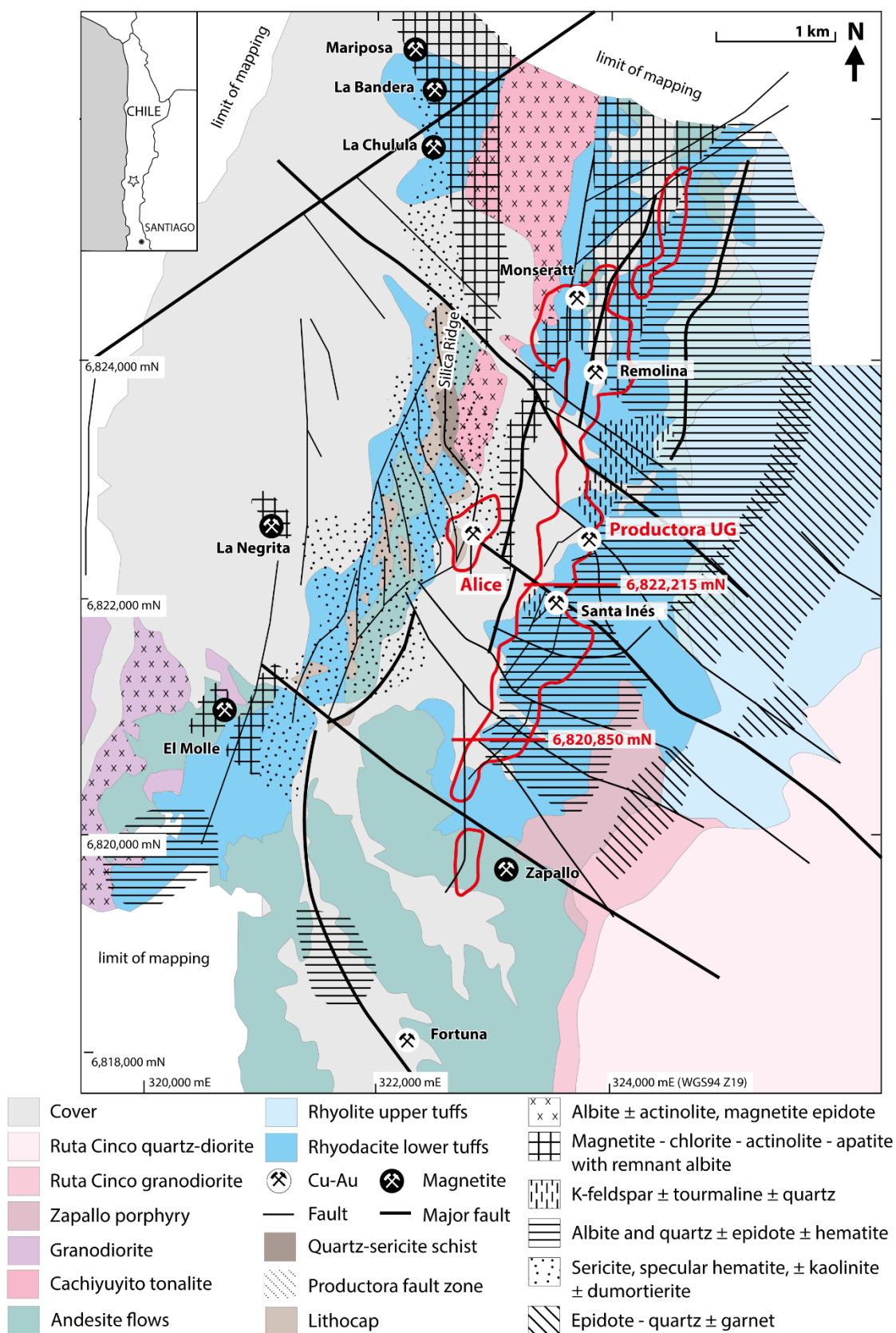




FIG. 8. Summary of the Productora camp scale paragenesis for major minerals. Paragenesis of the Productora breccia complex is separated into five stages. Reactivation of stage 2 is shown on the left of the diagram. Vertical variations in stage 3 breccia cement mineralogy are shown by triangles whose width is proportional to mineral abundance, strike variation is shown by triangle colour (black = section 6,822,215 mN, white = 6,820,850 mN). Relative intensity of mineralization is shown by continuous (strong) or dashed (weak) lines. Ruta Cinco and Cachiuyuyito events summarized from Fox (2000) and Ray and Dick (2002). Geochronology detailed in Tables 3 and 7.

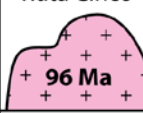

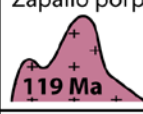



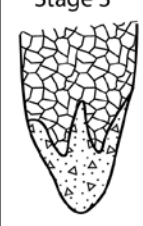
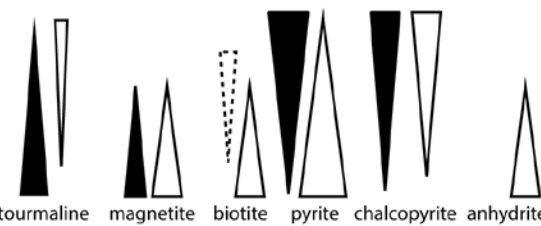
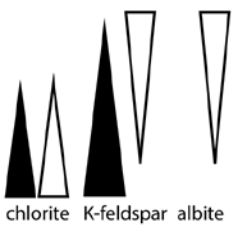




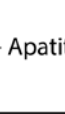
	Event	Veins and breccias	Alteration	Mineralisation
				Fe Cu Au Mo
PRODUCTORA BRECCIA COMPLEX	Ruta Cinco  96 Ma	Epidote ± pyrite ± chalcopyrite quartz veins ± gold	actinolite, magnetite, chlorite, sericite	
	Zapallo porphyry Mafic dykes  119 Ma			
	Alice Porphyry  121 Ma	↑ Calcite Pyrite, anhydrite, chlorite, epidote-chlorite  Quartz-pyrite ± chalcopyrite ± molybdenite Quartz-pyrite ± chalcopyrite Quartz-feldspar	Chlorite-sericite Albite ± epidote ± sericite  Potassic (biotite)	124-122 Ma 
	Stage 5	Calcite veins and calcite-cemented breccias		
	Stage 4	4A - Chlorite veins 4B - Chalcopyrite and pyrite veinlets 4C - Illite veins and alteration 4D - Epidote veins	4B - Muscovite selvage 4C - Pervasive illite 4D - Patchy epidote	
	Stage 3 	 tourmaline magnetite biotite pyrite chalcopyrite anhydrite	 chlorite K-feldspar albite	130-128 Ma 
	Stage 2 	Chaotic matrix supported breccias	Pervasive kaolinite- muscovite-pyrite	
	Stage 1 	Quartz-pyrite cemented breccia	Pervasive kaolinite-muscovite	
	Cachiuyuyito  130 Ma	Albite ± actinolite, magnetite and epidote veins	Albite, epidote, actinolite, chlorite	+ Apatite 



FIG. 9. Cross section at 6,822,215 mN showing interpreted distribution of breccia facies. Interpretation is based on graphic core logging, core photo library, drill hole data base (provided by Hot Chil Ltd), detailed hand specimen and thin section observations and QXRD data. Breccia cross-cutting relationships are indicated by the inclusion of clasts of earlier breccia stages. Stage 2 breccias are cross cut by stage 3 and also overprint stage 3 due to later fault reactivation. Variable breccia morphology (clast supported vs. cement supported) in stage 3 breccias are shown by fill pattern. Rhyolite lapilli tuff is shown with a light blue stippled pattern and rhyodacite lapilli tuff with a dark blue stippled pattern. The map includes a vertical scale from 400 m to 900 m, a horizontal scale from 323400 mN to 324000 mN, and a 100 m scale bar. A north arrow is located in the top right corner. The map shows several drill holes with labels: PRP0576, PRD0006, MET007, PRP0079, PRD0007, PRP0078, PRD0020, MET0008, PRP0069, MET0022, PRP0711, PRP0725, PRP0798, NS1D, and PRP0824. A dashed line indicates the 'top of sulfide' and a solid line indicates the 'limit of interpretation'. Areas with 'No drilling' are marked.

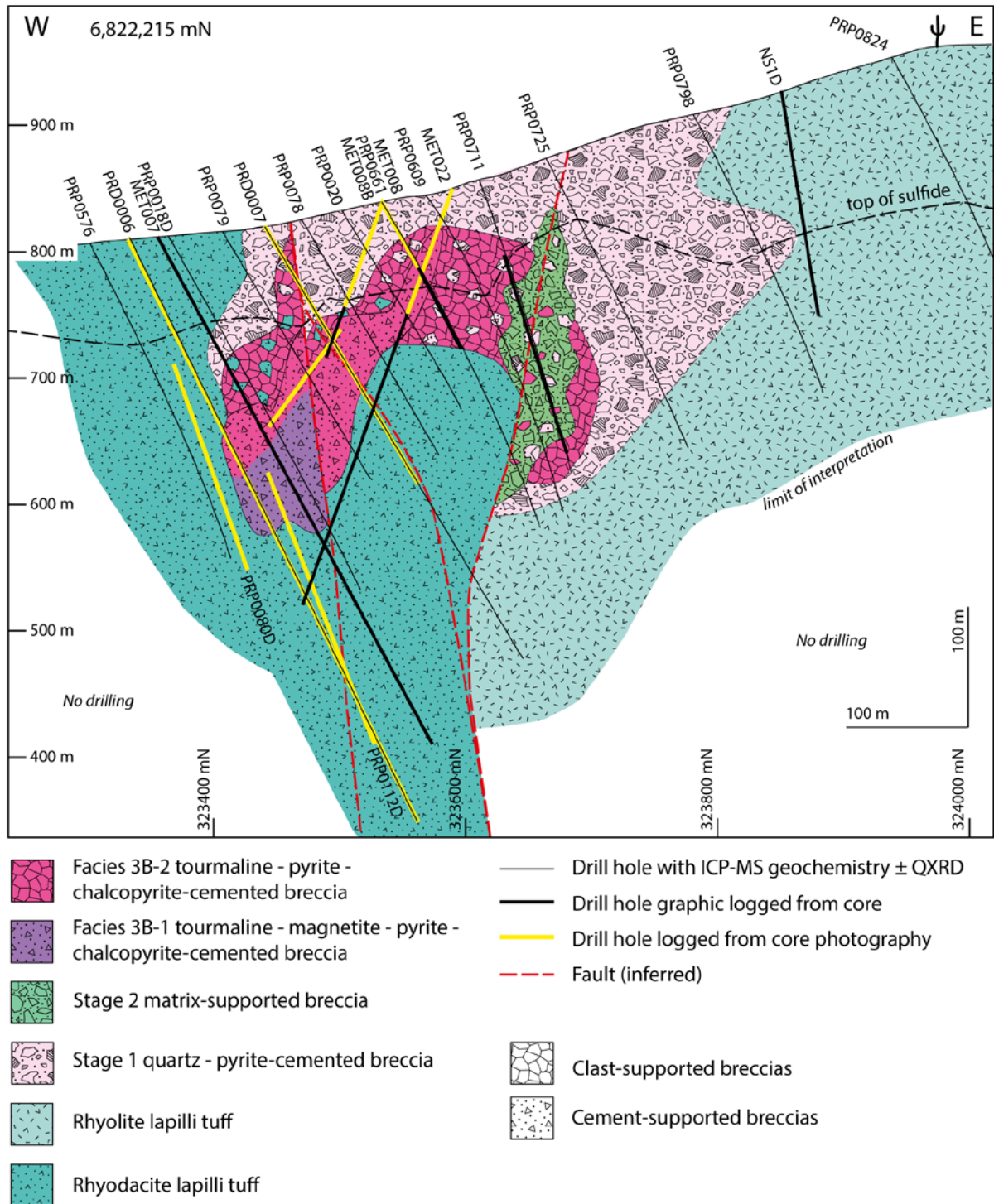


FIG. 10. Cross section at 6,820,850 mN showing interpreted distribution of breccia facies. Interpretation is based on graphic core logging, core photo library, drill hole data base (provided by Hot Chili Ltd), detailed hand specimen and thin section observations and QXRD data. Variable breccia morphology (clast supported vs. cement supported) in stage 3 breccias are shown by fill pattern.

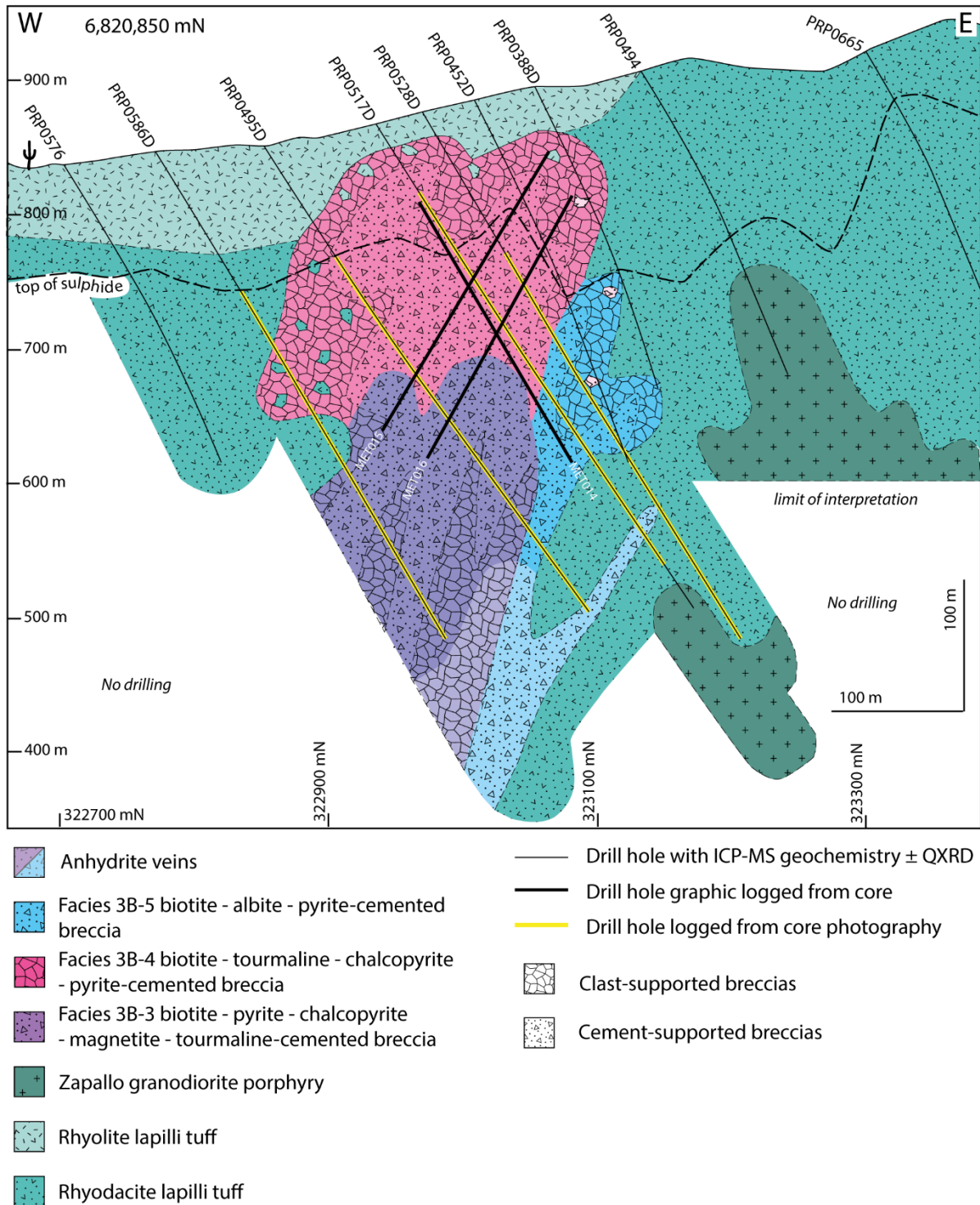




FIG. 11. A) Photograph of magnetite lens in hanging wall of fault exposed in drill pad cutting (322,798 mE, 6,822,405 mN). B) Photograph of massive magnetite with coarse apatite and minor actinolite (PR14AE198). C) Photograph of massive, coarse bladed actinolite and equant magnetite. D) Tourmaline vein and K-feldspar alteration cross cutting disseminated magnetite alteration (PRD0066, 115 m).

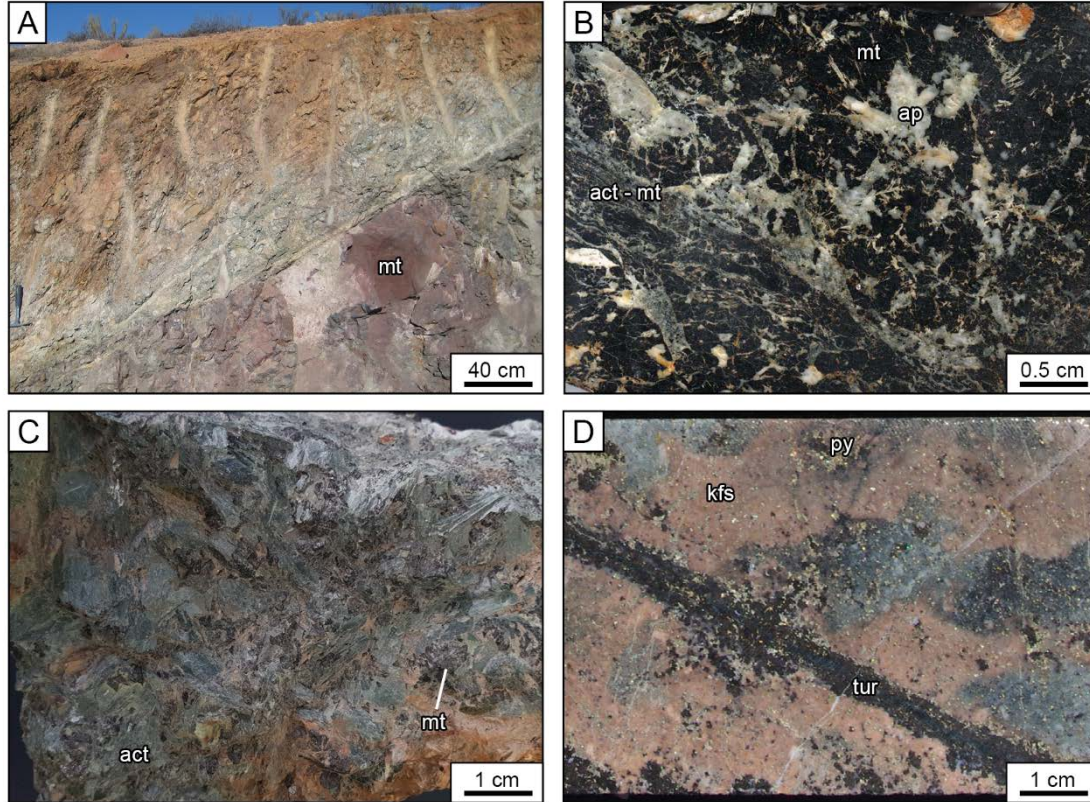




FIG. 12. Representative photos of stage 1 and 2 breccias. A) Surface hand specimen (PR14AE119) of stage 1 breccia showing matrix-supported texture with matrix of angular lithic fragments in quartz-pyrite cement, lithic clasts and matrix are intensely kaolinite-muscovite altered. B) Plane-polarized, transmitted light image of stage 1 feldspar-phyric, kaolinite-muscovite altered clasts with infill of quartz-pyrite cement and angular lithic matrix (PR14AE119). C) Core photo showing stage 2 polymict lithic fragments in matrix of rock flour and lithic fragments (PR14AE125, MET023 84.10 m). D) Transmitted light photomicrograph showing stage 2 polymict breccia clast in matrix-rich breccia with crosscutting chalcopyrite - covellite - tourmaline vein (PR14AE125). E) Photo of weakly cemented, broken drill core, typical of the most intensely brecciated domains of stage 2 (MET023, 97–103 m). F) Reflected light photo showing chalcopyrite with covellite replacement at grain boundaries in stage 2 breccia (PR14AE123, MET023 79.20 m). cpy = chalcopyrite, cv = covellite, fsp = feldspar, py = pyrite, tur = tourmaline, rt = rutile.

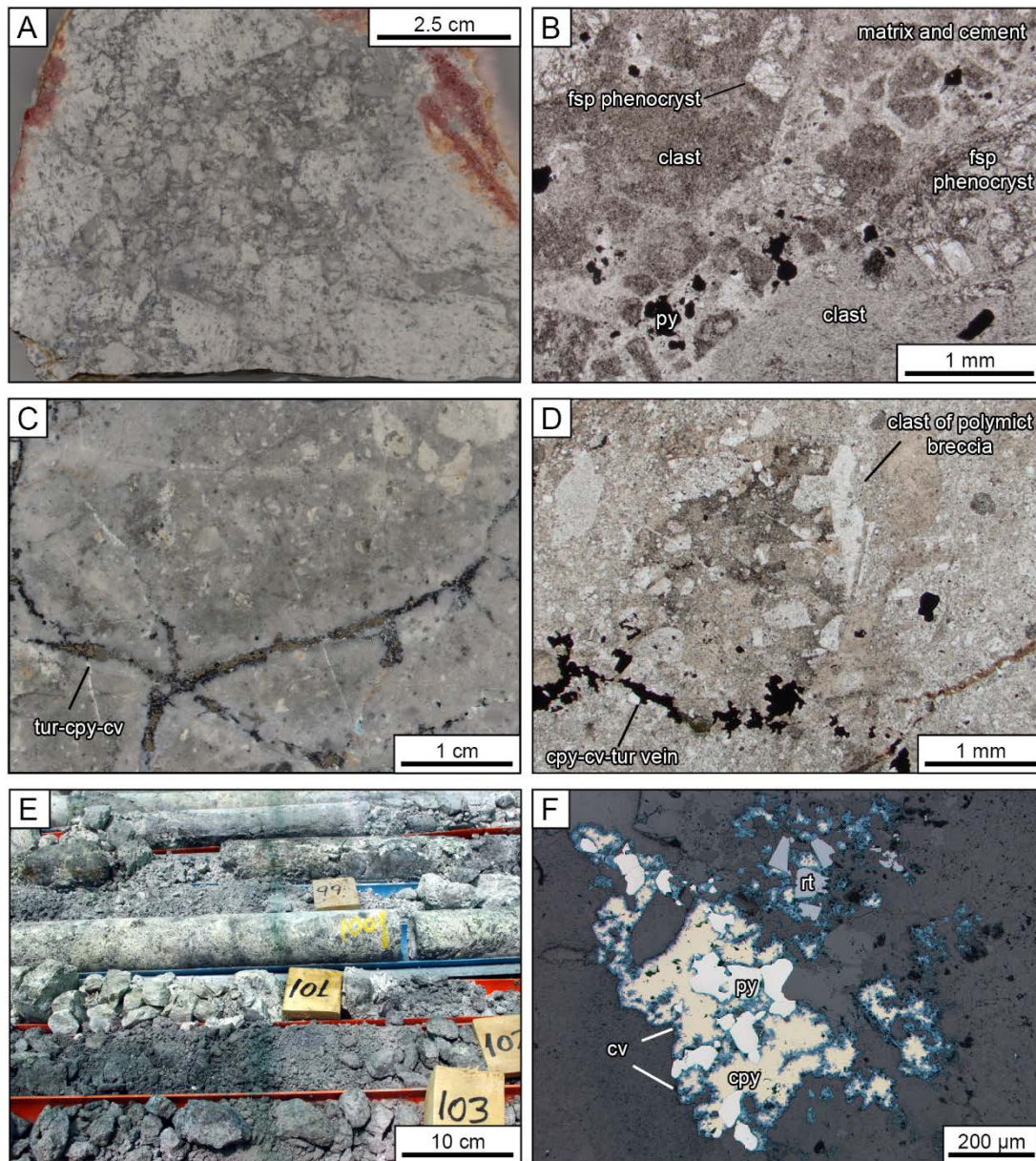


FIG. 13. Representative photos of stage 3A K-feldspar alteration. A) Core photo showing K-feldspar alteration halos to tourmaline-pyrite-chalcopyrite veins. Disseminated molybdenite occurs in vein halo (PR14AE113, PRP0066D 181.35 m). B) Core photo showing texturally destructive K-feldspar flooding with tourmaline-chalcopyrite veins (PRP0066D 171.80 m). cpy = chalcopyrite, kfs = K-feldspar, mo = molybdenite, py = pyrite, tur = tourmaline.

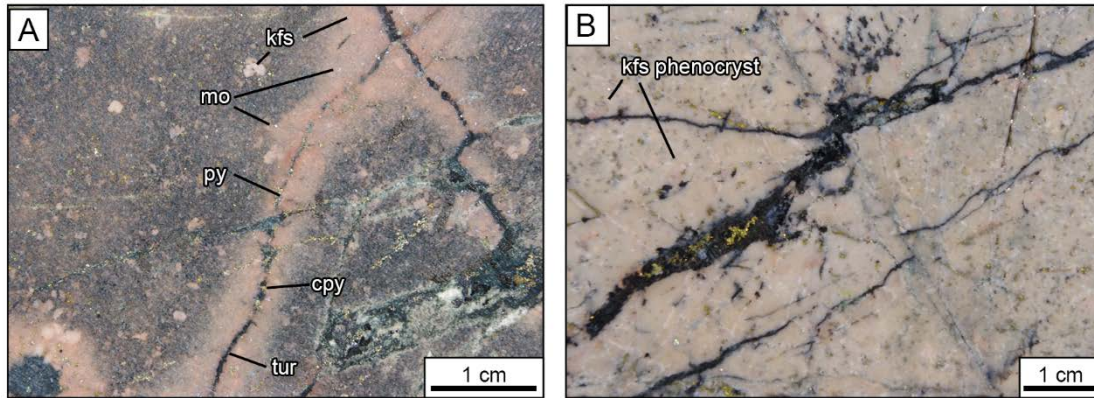


FIG. 14. Representative photos of stage 3B breccias. A) Facies 3B-1 breccia vein showing quartz altered selvage and intense K-feldspar alteration of host monomict rhyodacite breccia with replacement of protolith breccia infill by K-feldspar (PR14AE061, MET007 191.80 m). B) Facies 3B-3, clast-supported breccia with minor matrix (PR14AE162, MET015 239.60 m). C) Facies 3B-1 tourmaline-chlorite-quartz-chalcopyrite cemented breccia with feldspar-phyric coherent clasts (MET007 199 m). D) Facies 3B-3 biotite-dominant cement with secondary chlorite (PR14AE162). E) Facies 3B-5 half-core photo showing tourmaline - biotite-rich, chaotic, poorly-sorted, cement-supported and matrix-rich breccia with intense, texturally destructive K-feldspar alteration of clasts (PR14AE153, MET014 287.80 m). F) Facies 3B-3, hand specimen photo of anhydrite - chalcopyrite - tourmaline - pyrite vein (PR14AE174, MET016 316.40 m). Reflected light photos of facies 3B-1 showing G) concave grain boundaries between of both chalcopyrite and pyrite (PR14AE060) and H) subhedral magnetite with inclusions of, and interstitial, chalcopyrite and pyrite (PR14AE062, MET007 218.45 m).



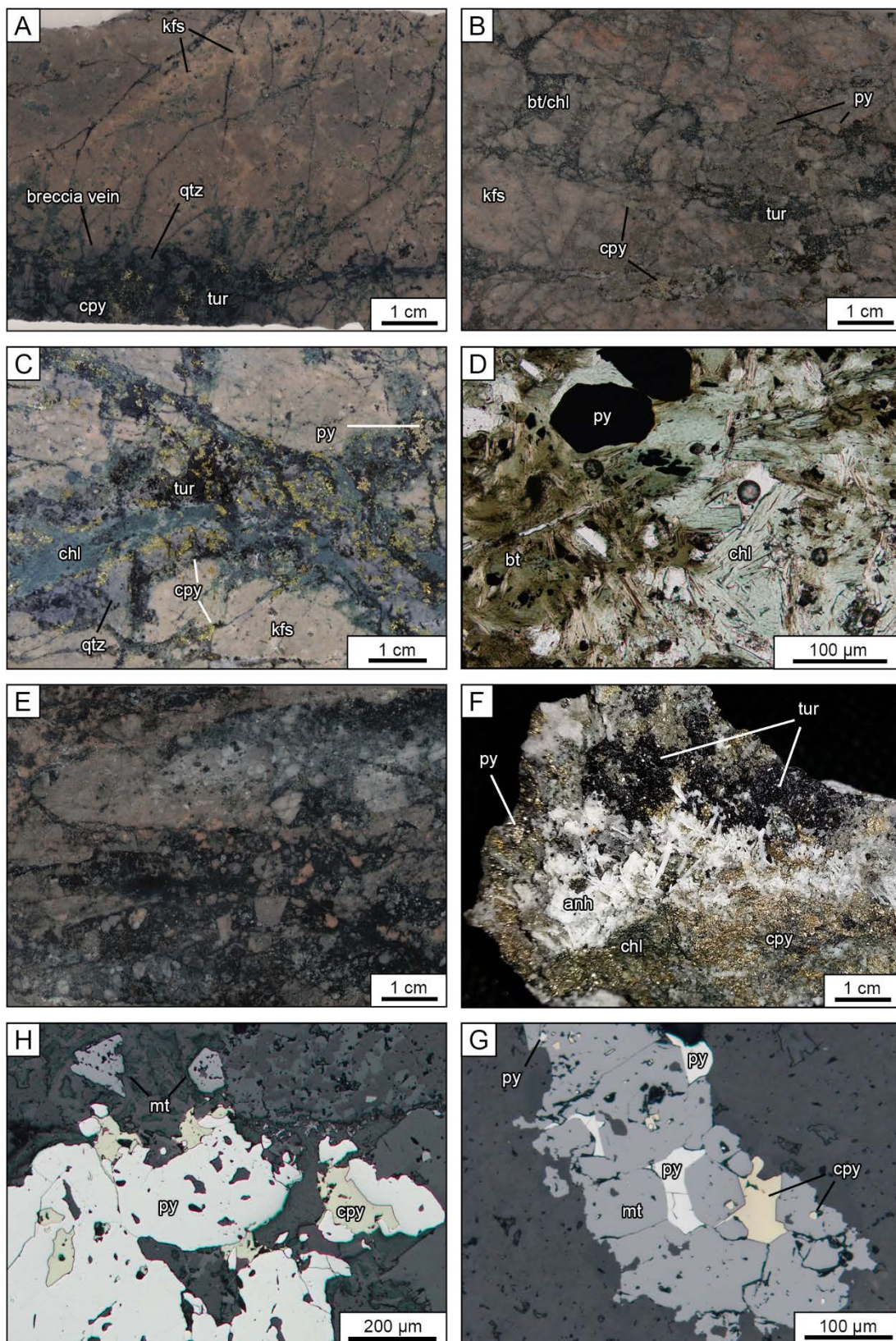




FIG. 15. Representative photos of stage 4 and 5 veins and alteration. A) Half-core photo showing stage 4A chlorite vein cross cutting tourmaline-K-feldspar veins and K-feldspar alteration of rhyodacite lapilli tuff (PR14AE048, MET007 441.33 m). B) Core photo showing weathered illite-chlorite-Cu-bearing clay-pyrite-goethite vein (PR14AE053, MET007 400.73 m). C) Half-core photo showing epidote-cemented breccia with cross cutting calcite veinlets (PR14AE100, PRP0064D 343.50 m). D) Half-core photo showing calcite-cemented breccia vein in rhyodacite lapilli tuff (PR14AE099, PRP0064D 2335.06 m). cal = calcite, chl = chlorite, ep = epidote, gt = goethite, kfs = K-feldspar, illite = illite, py = pyrite, tur = tourmaline.

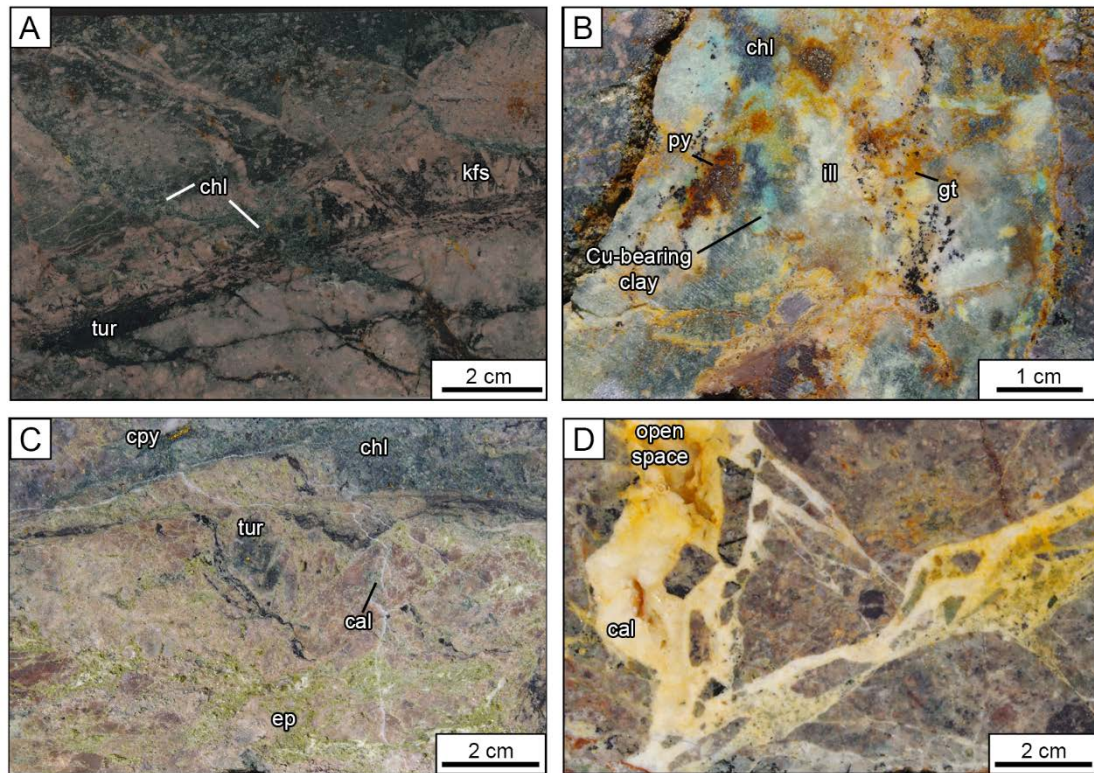


FIG. 16. Representative photos from core specimens showing major Alice Cu-Mo porphyry paragenetic vein relationships. A) Irregular, discontinuous early quartz - pyrite - chalcopyrite veins cross cut by later chlorite veins (PR14AE214, PXP0001D 195.7 m). B) Quartz veins with pyrite seam cross cuts earlier quartz - pyrite - chalcopyrite veinlets and is itself cross cut by anhydrite. Both are cross cut and displaced by chlorite-cemented fractures with muscovite selvages (PR14AE212, PXP0001D 175.8m). C) Quartz vein with central pyrite-chalcopyrite seam cross cut by massive quartz vein with molybdenite margins and grains of pyrite and chalcopyrite. Cross cut by irregular anhydrite vein (PR14AE213, PXP0001D 185.45m). D) Massive quartz - molybdenite - chalcopyrite vein cross cutting early quartz - K-feldspar vein and disseminated chalcopyrite (PXP0001D 154m). E) Massive pyrite vein cross cutting earlier quartz veinlets (PXP0001D 259m). F) Chlorite - chalcopyrite-cemented breccia with anhydrite overprint (PXP0001D 195m). G) Chlorite vein cross cut by epidote veinlets (PXP0001D 232m). anh = anhydrite, chl = chlorite, cpy = chalcopyrite, ep = epidote, kfs = K-feldspar, il = illite, mo = molybdenite, ms = muscovite, py = pyrite, qtz = quartz, tur = tourmaline.

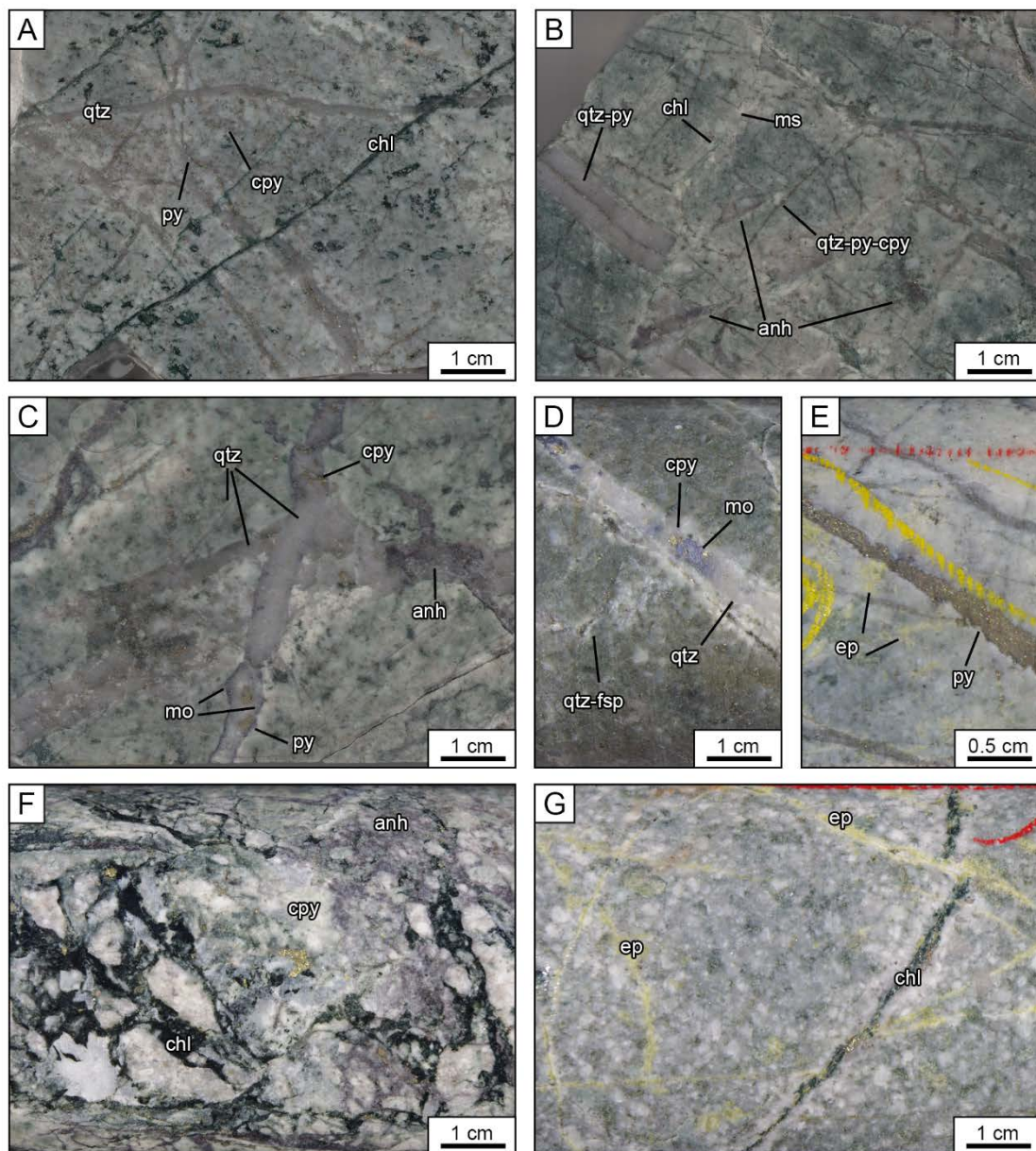




FIG. 17. Photos from Silica Ridge lithocap. A) Photo looking north along the northern segment of the disjointed lithocap. B) Hand specimen photo of chaotic, quartz-cement-supported, lithic breccia (PR14AE194, 322744 mE 6,822,481 mN, 826 m). C) Hand specimen photo of botryoidal chalcedony-cemented, lithic breccia with open space fill (PR14AE193, 322,746 mE 6,822,481 mN, 825 m).

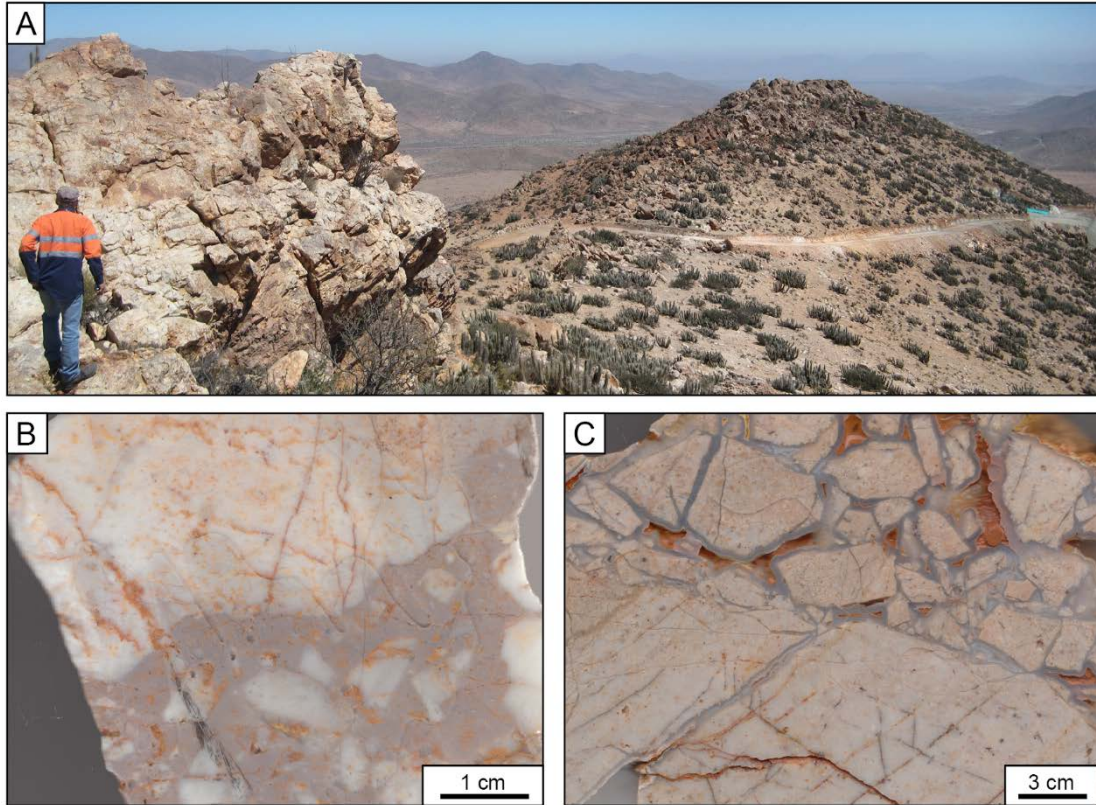


FIG. 18. Cross section at 6,822,215 mN (+/- 40 m window) with Cu grade shells modelled in 3D from Hot Chili Ltd whole rock assay database using Leapfrog Geo 3.1.0 (spheroidal interpolant; global trend with dip 75°, dip azimuth 285°, pitch 0; ellipsoid ratios maximum 3, intermediate 3, minimum 0; adaptive resolution 20). Simplified geology and mineralized breccia facies also shown with drill holes from assay database and intervals used for metal comparison.

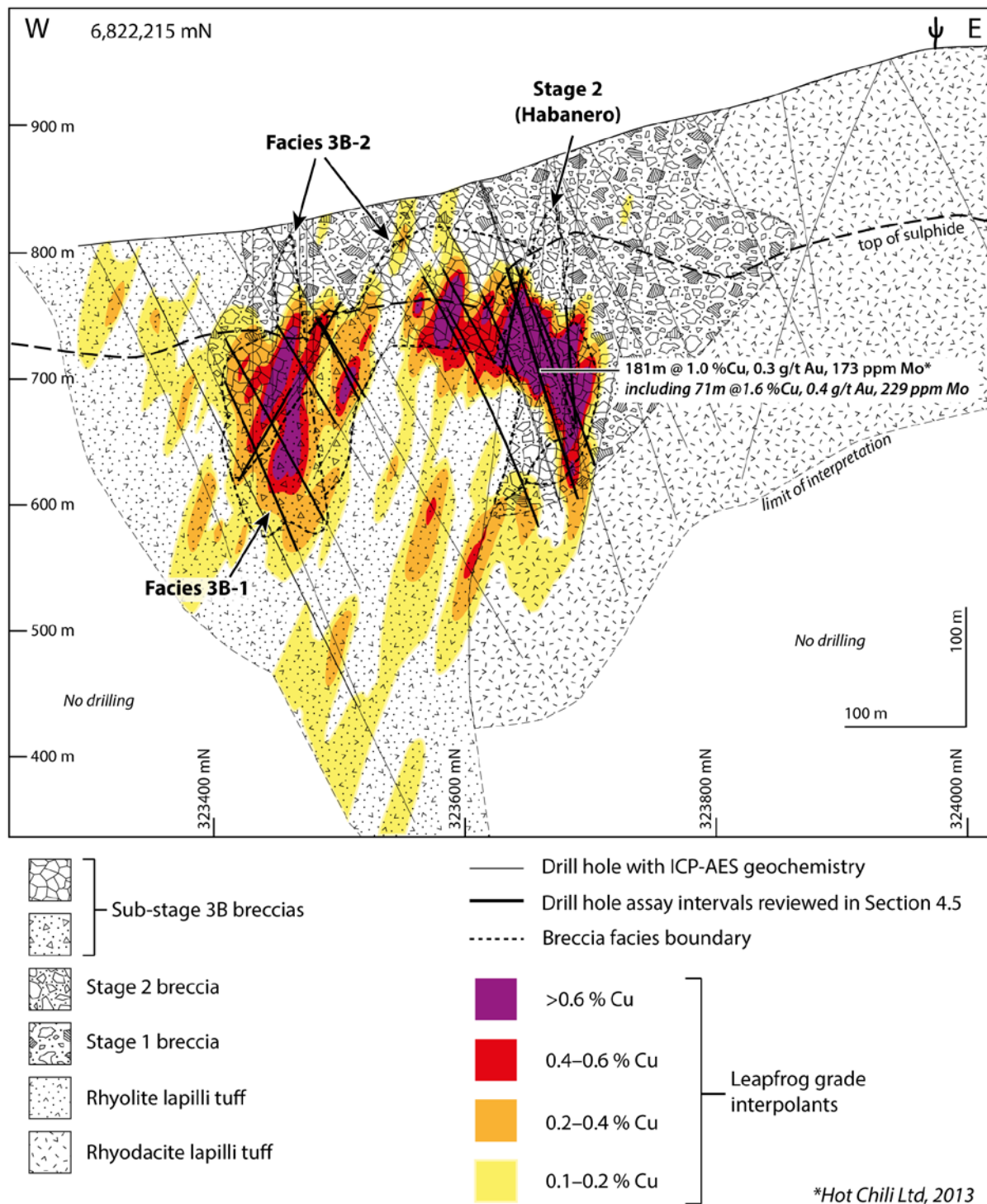


FIG. 19. Cross section at 6,820,850 mN (+/- 40 m window) with Cu grade shells modelled in 3D from Hot Chili Ltd whole rock assay database using Leapfrog Geo 3.1.0 (spheroidal interpolant; global trend with dip 75, dip azimuth 285, pitch 0; ellipsoid ratios maximum 3, intermediate 3, minimum 0; adaptive resolution 20). Simplified geology and mineralized breccia facies also shown with drill holes from assay database and intervals used for metal comparison.

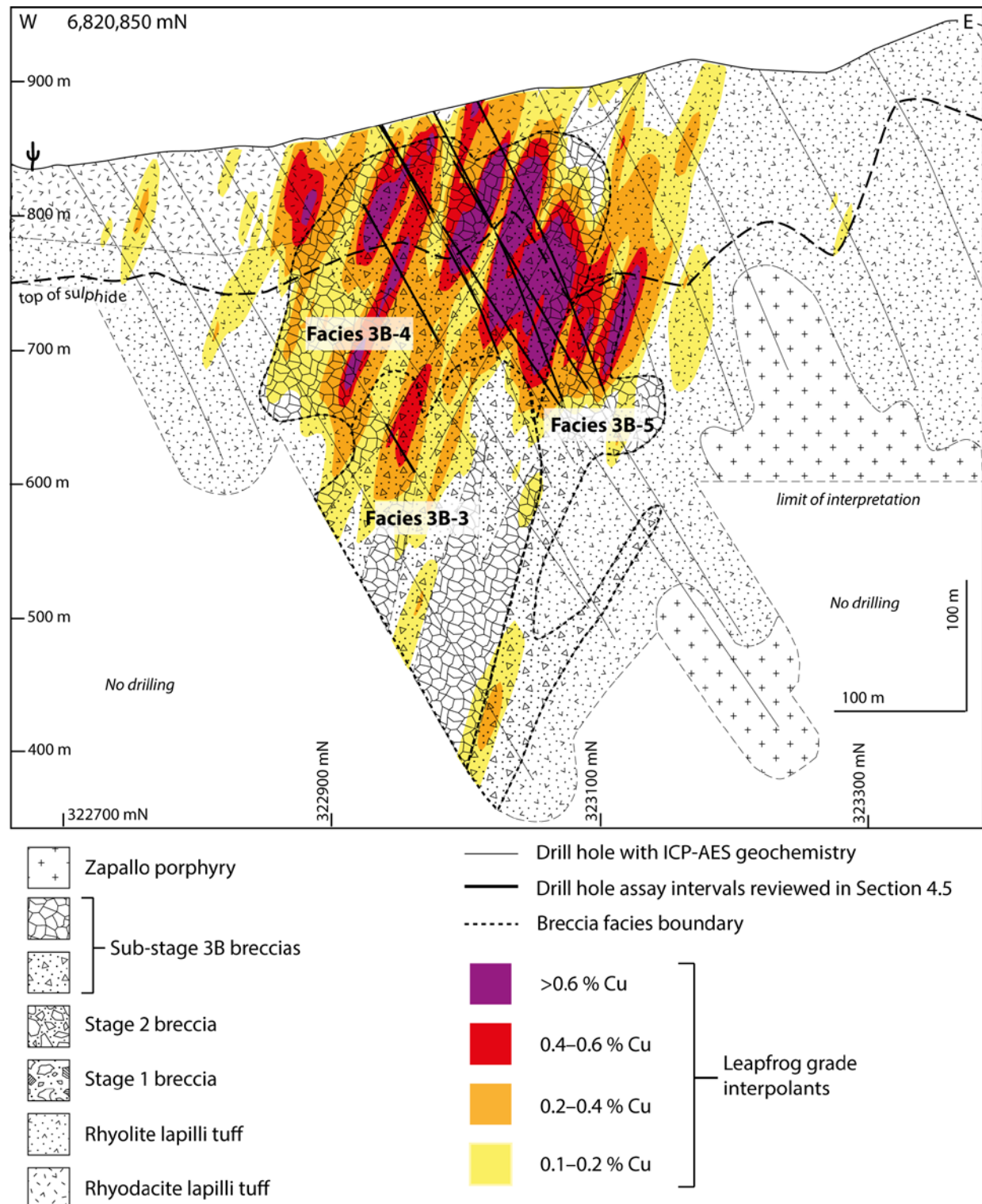




FIG. 20. Cross sections showing interpolants of estimated sulfide abundance from QXRD data combined with whole rock geochemical assays. A) Pyrite on section 6,822,215 mN. B) Chalcopyrite:pyrite ratio on section 6,822,215 mN. C) Pyrite on section 6,820,850 mN. D) Chalcopyrite:pyrite ratio on section 6,820,850 mN. Interpolants generated in Leapfrog Geo version 3.1.0 (spheroidal interpolant; global trend with dip 75°, dip azimuth 285°, pitch 0; ellipsoid ratios maximum 3, intermediate 3, minimum 0; adaptive resolution 20).

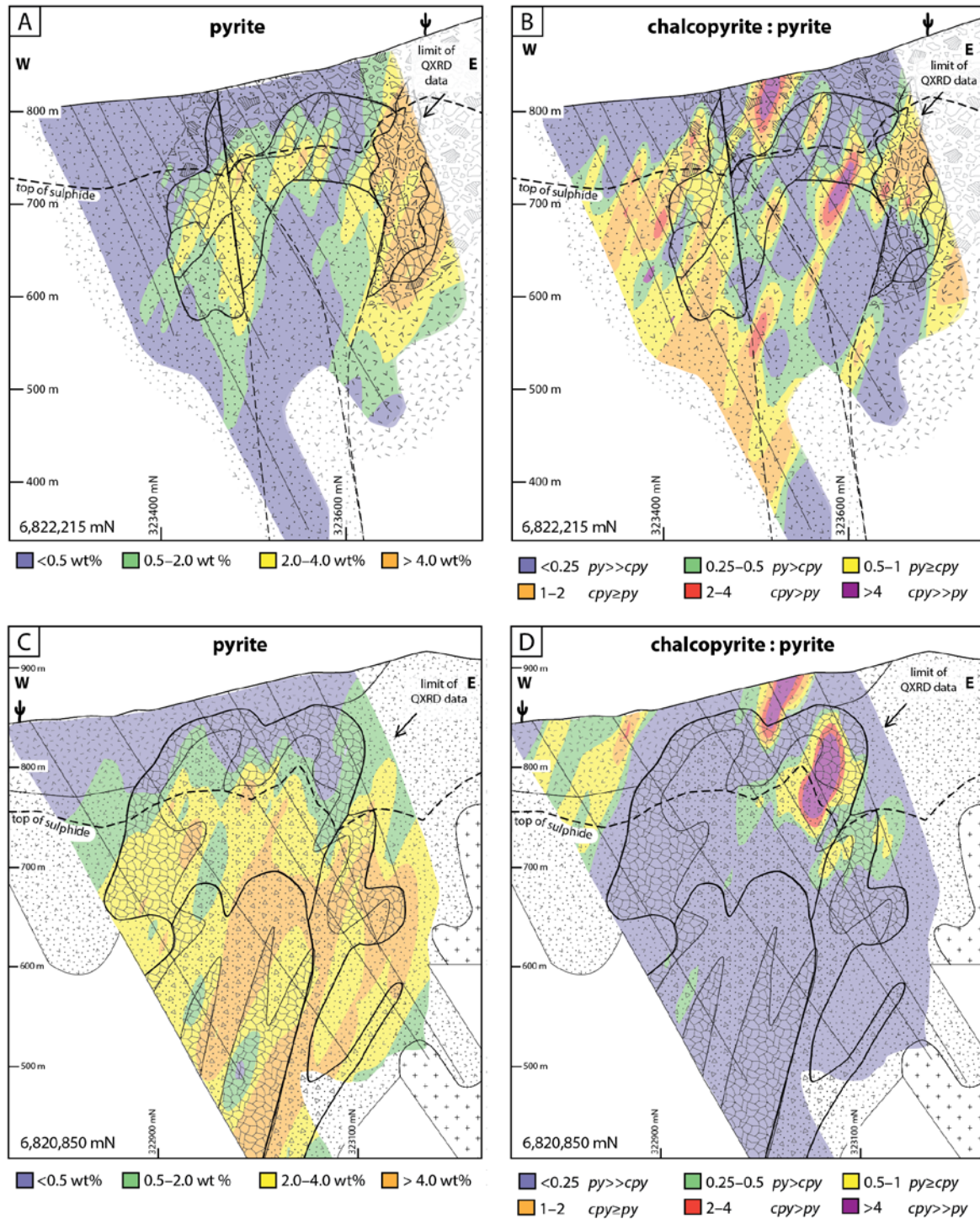


FIG. 21. Cumulative frequency histograms to show  $\delta^{34}\text{S}$  data. A) Data from Fox (2000). B) All new data from this study with paragenetic stage indicated by pattern. C) Stage 3 chalcopyrite and D) stage 3 pyrite from the current study. Data from this study define a similar range to that of Fox (2000). Values for  $\delta^{34}\text{S}$  from chalcopyrite are more negative than from pyrite. There is a subtle shift in  $\delta^{34}\text{S}$  toward more negative values from south to north in both the chalcopyrite and pyrite data.

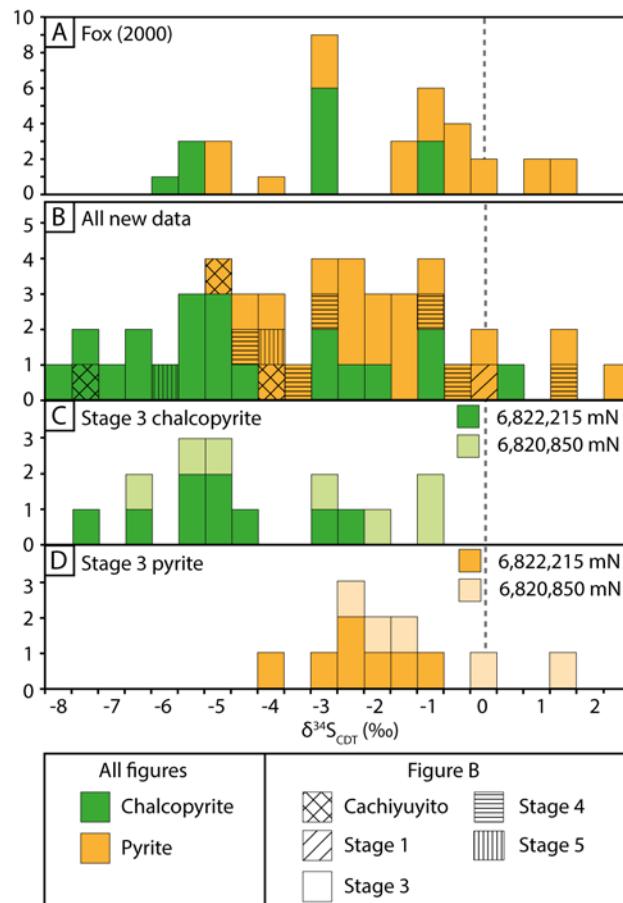


FIG. 22. Compilation of  $\delta^{34}\text{S}$  values for sulfide minerals, mostly pyrite and chalcopyrite, from selected IOCG, manto-Cu, vein, skarn, magnetite-apatite and porphyry deposits in northern Chile and southern Peru. Figure modified from Sillitoe (2003), data from Ripley and Ohmoto (1977), Ohmoto and Rye (1979), Taylor (1987), Vivallo and Henríquez (1998), Leidli (1998) in Hopper and Correa (2000), Lieben et al. (2000), Marschik and Fontbote (2001), Ramirez et al. (2006), Benavides et al. (2007), de Haller and Fontbote (2009), Rieger et al. (2012). Values are centered close to zero ‰, indicating a predominantly magmatic sulfur source if one assumes conditions are relatively reduced and aqueous sulfur is sulfide ( $\text{H}_2\text{S}$ ,  $\text{HS}^-$ )-dominated (Barton, 2014). Large deviations at Raul-Condestable are interpreted to indicate reduction of evaporitic or seawater sulfate (Ripley and Ohmoto, 1977; de Haller et al., 2002) and biogenic sulfur (de Haller et al., 2002).

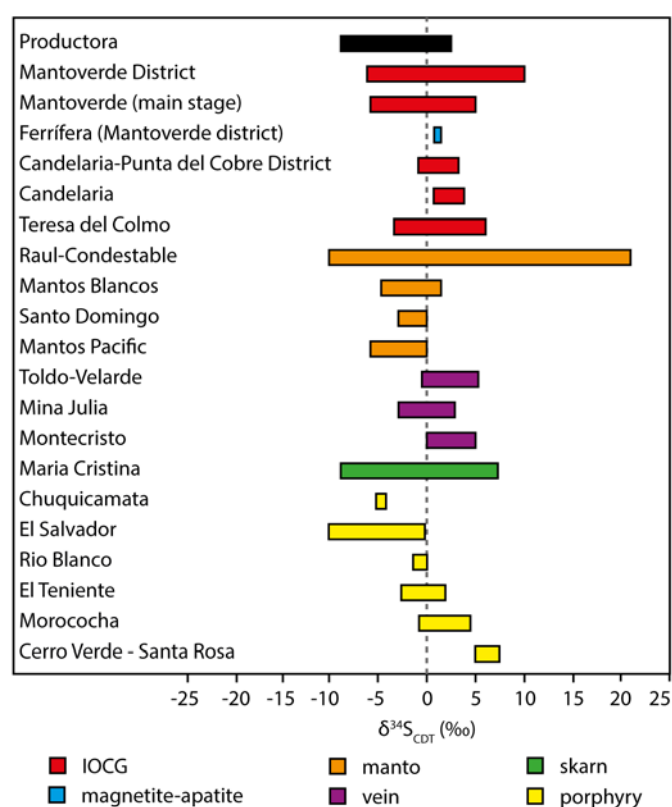


FIG. 23. Initial  $^{87}\text{Sr}/^{86}\text{Sr}$  isotopic data for tourmaline from Productora, compared to other Mesozoic deposits in northern Chile, as well as major crustal rocks of northern Chile and Mesozoic sea water (Viezer et al. 1999). Diagram modified from Cooke et al. (2011). Data sourced from <sup>1</sup>Sillitoe (1987), <sup>2</sup>Ramirez et al.(2008), <sup>3</sup>Rogers and Hawkesworth (1989) and <sup>4</sup>McNutt et al. (1975), and Lucassen et al. (2002), Morata and Aguirre (2003), Morata et al. (2008) and Girardi (2014).

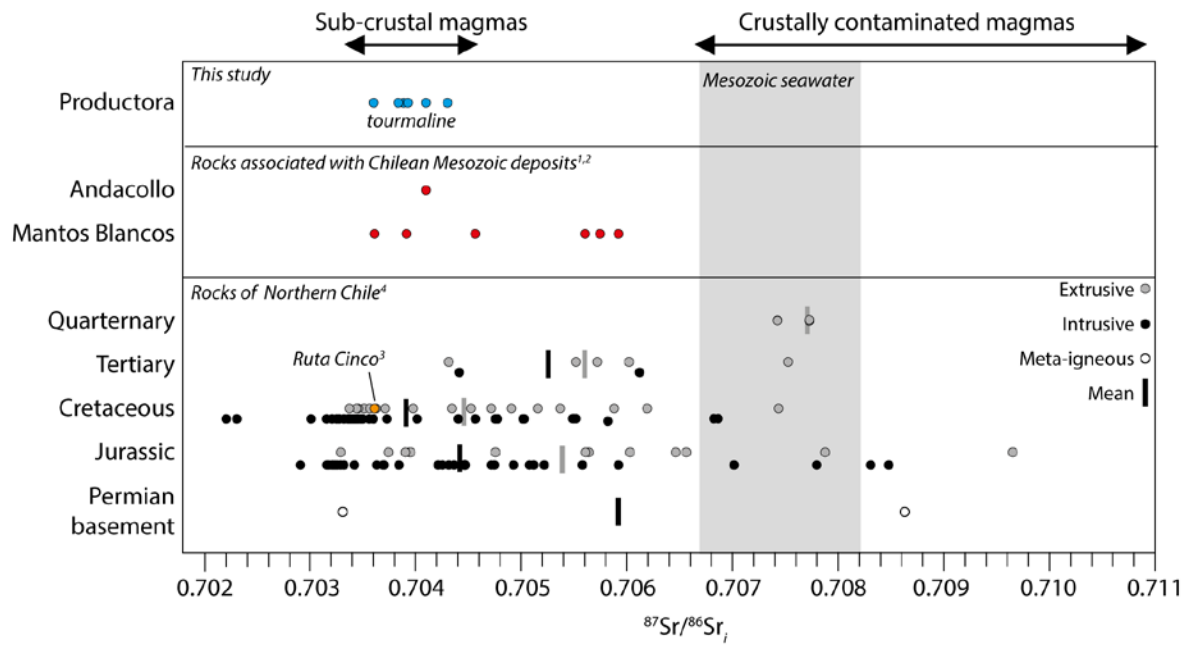




FIG. 24. Schematic cross sections illustrating key aspects of the genetic model for Productora. A) Regionally, thick sequences of subaerial volcanic rocks were deposited in the Mesozoic magmatic arc under extensional to transtensional conditions with coeval plutonism. B) Locally, intrusion of the Cachiuyuito stock is spatially and temporally associated with large-scale sodic-calcic alteration, magnetite-apatite mineralization (fluid source and evolution unconstrained) and emplacement of the Productora magmatic-hydrothermal breccia complex and Cu-Au-Mo mineralization. Local faults associated with the regional Atacama Fault Zone were active throughout. C) Emplacement of the Alice porphyry and associated porphyry Cu-Mo mineralization and advanced argillic lithocap (absolute age undetermined). Intrusion of barren Zapallo porphyry and Ruta Cinco batholith. Current erosion level indicated.

